Wetland monitoring with Global Navigation Satellite System reflectometry

Son V. Nghiem[1], Cinzia Zuffada[1], Rashmi Shah[1], Clara Chew[1], Stephen T. Lowe[1], Anthony J. Mannucci[1], Estel Cardellach[2], G. Robert Brakenridge[3], Gary Geller[1,4], and Ake Rosenqvist[5]

[1]Jet Propulsion Laboratory, California Institute of Technology, Pasadena, California, USA, [2]Institut de Ciències de l'Espai/CSIC-IEEC, Barcelona, Spain, [3]Community Surface Dynamics Modeling System, Institute of Arctic and Alpine Research, University of Colorado Boulder, Boulder, Colorado, USA, [4]Group on Earth Observations (GEO), Geneva, Switzerland, [5]solo Earth Observation (soloEO), Tokyo, Japan

Abstract Information about wetland dynamics remains a major missing gap in characterizing, understanding, and projecting changes in atmospheric methane and terrestrial water storage. A review of current satellite methods to delineate and monitor wetland change shows some recent advances, but much improved sensing technologies are still needed for wetland mapping, not only to provide more accurate global inventories but also to examine changes spanning multiple decades. Global Navigation Satellite Systems Reflectometry (GNSS-R) signatures from aircraft over the Ebro River Delta in Spain and satellite measurements over the Mississippi River and adjacent watersheds demonstrate that inundated wetlands can be identified under different vegetation conditions including a dense rice canopy and a thick forest with tall trees, where optical sensors and monostatic radars provide limited capabilities. Advantages as well as constraints of GNSS-R are presented, and the synergy with various satellite observations are considered to achieve a breakthrough capability for multidecadal wetland dynamics monitoring with frequent global coverage at multiple spatial and temporal scales.

1. Introduction

Wetland dynamics alter both atmospheric methane and terrestrial water storage. The Intergovernmental Panel on Climate Change's Fifth Assessment Report (IPCC AR5) highlights the role of wetlands as a key driver of methane (CH_4) emission, which is more than an order of magnitude stronger than carbon dioxide as a greenhouse gas in the centennial timescale. Among the multitude of CH_4 emission sources (hydrates, livestock, rice cultivation, freshwaters, landfills and waste, fossil fuels, biomass burning, termites, geological sources, and oxidation reactions in soils), wetlands constitute the largest single contributor (~30%) and with the widest uncertainty range of 177–284 Tg(CH_4) yr^{-1} according to the IPCC estimate [*Intergovernmental Panel on Climate Change (IPCC)*, 2013].

CH_4 in the Earth's atmosphere has varied peculiarly in recent decades. Whereas CH_4 concentration was stable for a decade starting in the late 1990s, atmospheric measurements indicated a subsequent increase beginning in 2007. While the exact drivers of such renewed growth are still unclear, a bottom-up estimation [*IPCC*, 2013] suggests that climate-driven fluctuations of methane emissions from natural wetlands may be the main drivers of the global interannual variability.

The increase or decrease in wetland extent is dependent on the regional wetland hydrology, which can be significantly impacted by changes in temperature and precipitation. This complexity inflicts a low confidence in quantitative projections of wetland CH_4 emission from models and ecosystem warming simulations. The spatial distribution and the temporal variability of wetlands remain poorly constrained, despite the existence of applicable remote sensing products derived with algorithms using data from an array of past and present satellite sensors [*Papa et al.*, 2010; *IPCC*, 2013].

Wetlands are also highly susceptible to climate change leading to wetland collapse. Such wetland destruction could decrease the terrestrial water storage capacity and thus contribute to sea level rise. Consequently, this would exacerbate problems caused by coastal flooding [*Neumann et al.*, 2015] and saltwater intrusion [*Chen et al.*, 2016]. A complete and consistent dynamic map of global wetlands should

therefore be obtained, and the international *Ramsar Convention* [2015], named after the city of Ramsar in Iran where the Convention was signed, calls for a global wetlands inventory and impact assessment.

This wetland information gap has also long been recognized in the International Geosphere Biosphere Programme Global Analysis, Integration and Modeling report, which states "Wetland extent: The largest gap in wetland characterization is the size of wetlands themselves, both in space and time. The level of flooding and the areal extent of wetlands is the largest uncertainty in applying models of wetland function to models of the global system. Both the temporal and areal extent of wetland flooding should be characterized in terms of hectare-days. An additional factor is the phasing of flooding (i.e., continuous or intermittent). These issues are not adequately addressed in land cover compilations and terrestrial ecosystem models" [*International Geosphere-Biosphere Programme-Global Analysis, Interpretation and Modelling (IGBP-GAIM)*, 1996].

While the International Geosphere-Biosphere Programme-Global Analysis, Interpretation and Modelling (IGBP-GAIM) report highlighted the progress made in the 1980s leading to a classic global digital data set of wetlands [*Matthews and Fung*, 1987], it also noted the insufficient wetland characterization despite various remote sensing approaches than available, including microwave radars, radiometers, and multispectral sensors. A decade later, a review of spaceborne synthetic aperture radar (SAR) potential to support the Ramsar Convention [*Rosenqvist et al.*, 2007] underlined the aptness of L band SAR to map and monitor wetland characteristics, in particular, below-canopy flooding in freshwater wetlands and raised an awareness among the science community of the importance of wetlands and climate. Considerable limitations nevertheless remain [*Papa et al.*, 2010; *IPCC*, 2013] before a major breakthrough in the dynamic mapping of global wetlands can be realized.

To advance the capability for monitoring the dynamics of wetland extent, we present here an innovative approach using Global Navigation Satellite Systems Reflectometry (GNSS-R) for global wetland mapping in synergy with the existing capability, not only as a static inventory but also potentially as a temporal data set. After a review of current satellite methods for wetland mapping, we describe GNSS-R and then demonstrate its use for wetland observations.

We use GNSS-R data from an aircraft field campaign across the Catalonia wetland in the Ebro River Delta in Spain, analyze initial satellite results from the TechDemoSat-1 (TDS-1) mission, and examine future satellite capabilities such as the Cyclone Global Navigation Satellite System (CYGNSS) and other potential missions still in the planning stages. Prior to such missions, it is important for the scientific community to consider the potential, constraints, and specific observations that are needed to address global wetland extent and dynamics.

2. Current Methods for Wetland Mapping

The IGBP-GAIM report [*IGBP-GAIM*, 1996] evaluates advantages and limitations of various remote sensing methods for wetland mapping. These include an array of different instruments systematically grouped into six categories: optical coarse resolution (e.g., Advanced Very High Resolution Radiometer, AVHRR), optical fine resolution (e.g., Landsat, Satellite Pour l'Observation de la Terre, SPOT; Indian Remote Sensing Satellite Linear Imaging Self-Scanning System, IRS/LISS; Advanced Earth Observing Satellite Advanced Visible and Near Infrared Radiometer, ADEOS/AVNIR), optical hyperspectral sensors (e.g., Airborne Visible/Infrared Imaging Spectrometer, AVIRIS), passive microwave radiometers (e.g., Scanning Multichannel Microwave Radiometer, SMMR; Special Sensor Microwave/Imager, SSM/I), active microwave radars (e.g., European remote sensing satellite, ERS; Japanese Earth Resources Satellite, JERS; RADARSAT synthetic aperture radars, SAR), and altimetry (e.g., Seasat, Geosat, ERS, and TOPEX/Poisedon). Since the late 1990s, for all of those satellite instrument categories, numerous additional sensors have been launched and operated and their data have been applied to map wetlands and observe their changes [e.g., *Toyra et al.*, 2002; *Melack*, 2004; *Henderson and Lewis*, 2008; *Papa et al.*, 2010; *Silva et al.*, 2010; *Watts et al.*, 2012; *Rokni et al.*, 2014; *Chapman et al.*, 2015; *Hestir et al.*, 2015; *Romanov and Khvostov*, 2015; *Moser et al.*, 2016].

In particular, the Japan Aerospace Exploration Agency (JAXA) has a long-term program for systematic observations of tropical and boreal wetlands using their successive L band SAR missions (JERS-1 SAR, ALOS PALSAR, and ALOS-2 PALSAR-2) [*Japan Aerospace Exploration Agency Earth Observing Research Center*,
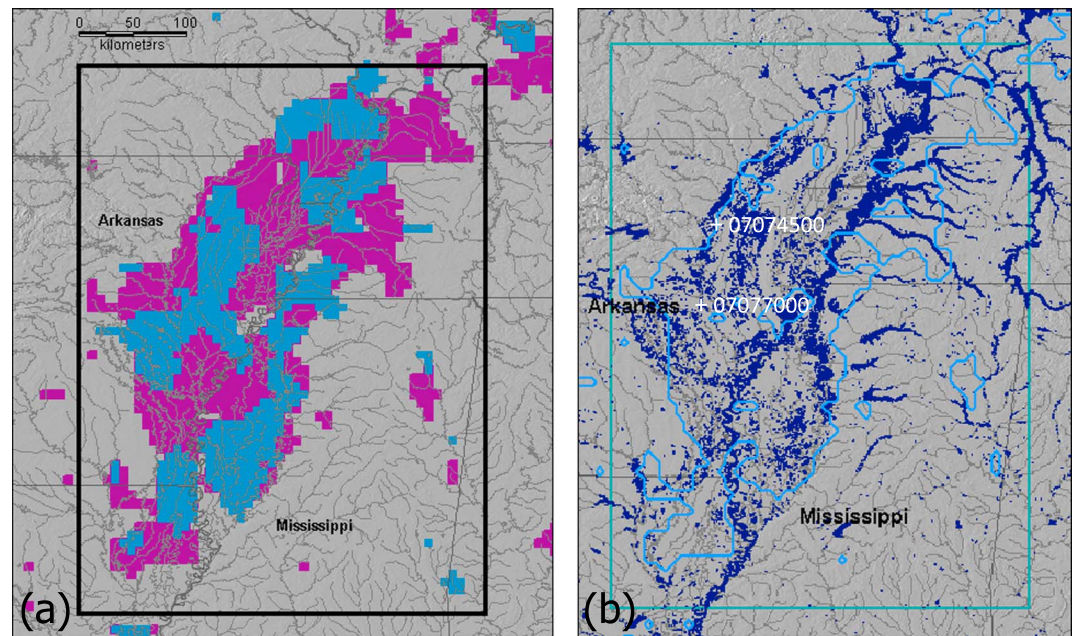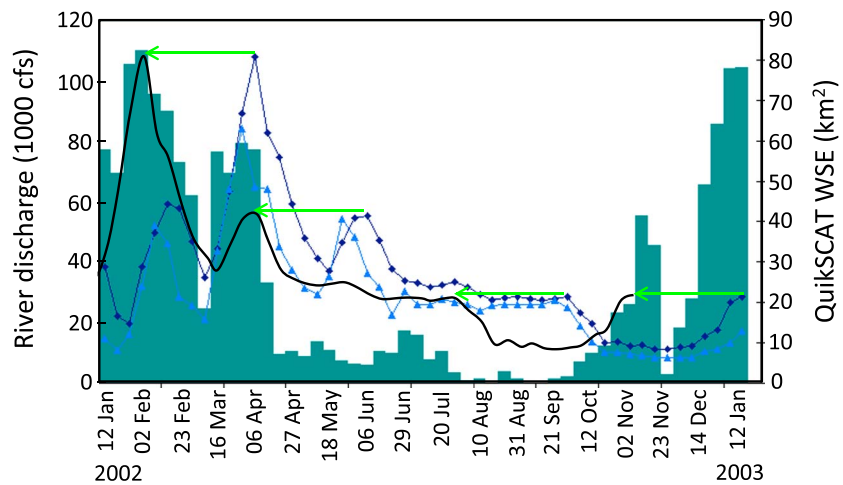
Figure 1. Mississippi wetlands observed by (a) QuikSCAT WSE for weekly change monitored in the week ending 9 November 2002 (magenta) with respect to the largest in the week ending 2 February 2002 (blue, much of which is beneath the magenta) and (b) by MODIS as an inventory compiled over time (right). The rectangle defines the study area.

2016]. Observations are typically undertaken in wide-beam (ScanSAR) observation mode at medium (100 m) spatial resolution and with a temporal repetition frequency of 42–46 days (JERS-1 44 days; ALOS 46 days; and ALOS-2 42 days). Outcomes from a parallel international science program include basin- and subbasin-scale wetland inundation maps from Alaska [*Whitcomb et al.*, 2007], South America [*Chapman et al.*, 2015], Africa [*Rebelo*, 2015], and Southeast Asia [*Hoekman*, 2007]. Results also demonstrate how flood duration maps derived from L band SAR can be coupled with CH_4 emission models to provide basin-wide estimates of annual CH_4 discharges [*Rosenqvist et al.*, 2002]. A major limiting factor is the temporal resolution of the radar observations, as even a repetition frequency of 6 weeks (ALOS-2) is insufficient to accurately characterize the complex and highly dynamic flooding patterns across river basins.

The utility of C band SAR for wetlands monitoring is largely conditioned by the shorter (5.6 cm) wavelength, which does not allow for uniform detection of standing water in densely vegetated or forested wetlands. Nevertheless, ERS, Envisat, and RADARSAT data have been used to monitor lower vegetation in artificial wetlands, such as irrigated rice [*Le Toan et al.*, 1997; *Nguyen et al.*, 2009, 2015; *Kumar et al.*, 2016] and to map lake types in the Brazilian Pantanal [*Costa and Telmer*, 2006]. Also, C band altimeters have proven to be useful for measuring changes in water levels in lakes, (large) rivers, and wetlands [*Birkett*, 1998].

There are as well recent observational strategies using other existing sensors. Noted here is a new method based on polarization ratio anomalies using satellite data from an azimuthally scanning Ku band scatterometer [*Nghiem*, 2001; *Brakenridge et al.*, 2005]. This method is adapted to delineate wetland extent and monitor wetland dynamics over a continental scale, and an example is presented here for Mississippi Valley wetlands. The study area (Figure 1) includes the lower Mississippi River meandering through a broad alluvial floodplain. This area is characterized by high water tables, oxbow lakes, wetlands, and back swamps. It includes ~256,500 km^2 of the lower Mississippi floodplain, primarily in Arkansas and Mississippi.

Applying the polarization ratio method to data acquired by the SeaWinds scatterometer aboard the QuikSCAT satellite, the dynamics of wet surface extent (called WSE henceforth) were monitored in the lower Mississippi valley on a weekly basis throughout 2002. Figure 1a presents the changes observed in the week ending 9 November 2002 (in magenta) with respect to the largest water extent in the week ending 2 February 2002 (in blue, much of which is beneath the magenta). Figure 1b shows a composite of all wet surface areas, observable by a multiband method using Moderate-resolution Imaging Spectroradiometer (MODIS) satellite data [*Brakenridge and Anderson*, 2006] over the time from 2000 to early 2003, together with the outline of the

Figure 2. Comparison of QuikSCAT weekly observations of wet surface extent (WSE, dark green vertical bar plot) over Mississippi wetlands (Figure 1) with USGS river discharge from gauging stations (ID 07077000 with diamond mark curve and 07074500 with triangle mark curve). Both stations had a similar seasonal change in river discharge, but that from station 07074500 had smaller values and earlier response since it was upstream of station 07077000. Light green arrows denote the shift by ~2 months between wetland change and stream flow at station 07077000, for which there is a high correlation between river and wetland response (black curve versus green bar plot, respectively), illustrating the wetland storage capacity in holding back the water.

maximum extent of QuikSCAT wet surface. This comparison shows that the QuikSCAT maximum WSE is quite consistent with the MODIS surface water compilation under clear-sky conditions with a higher resolution but with a smaller unobscured coverage from data collected at different times in different years.

To study the hydrological implications of the wetland dynamics observed by QuikSCAT, we used river discharge data from the United States Geological Survey (USGS) gauging stations (IDs 07077000 and 07074500) along the White River, a tributary that flows in the Mississippi floodplain. During year 2002, QuikSCAT WSE fluctuated up to 82,433 km^2, indicating a large dynamic range of the seasonal cycle of surface water. The variations in QuikSCAT WSE in the Mississippi basin were examined over the full year period by comparing them to discharge data from the in situ gauging (Figure 2). We found a consistency between the QuikSCAT WSE and the discharge data when the discharge curve is moved back in time by approximately 2 months (indicated by green arrows in Figure 2). Results from this study show that the timescale of the WSE variations is typically 1 to 2 months, which requires semimonthly measurements to track the wetland dynamics in this region. This case illustrates the terrestrial water storage capacity of the Mississippi wetlands in holding and later releasing water into the river system. It is presented as an example of the needed dynamic characterization of wetlands over large areas and on a global basis that could help constrain their role in both the water cycle and in geochemical processes, such as CH$_4$ emission.

3. The GNSS-R Technique

Despite the past work and multiple applicable sensors, a consistent global characterization of both the spatial distribution and temporal variability of wetlands worldwide has not yet been attained. New methods are needed in order to advance the capability to monitor global wetland dynamics with the needed spatial and temporal coverage. To address this need, we consider the abundance of current and future satellite systems used for navigation and positioning. These include: the NAVSTAR Global Positioning System (GPS), the GLObal NAvigation Satellite System (GLONASS), the European Space Agency Galileo GNSS, the Indian Regional Navigation Satellite System (IRNSS), the Quasi-Zenith Satellite System (QZSS), GPS and geo-augmented navigation system (GAGAN), and the Chinese BeiDou Navigation Satellite System (BDS). Extensive real-time global data from these GNSS systems offer an innovative approach toward sensing ground surface characteristics with temporal and spatial coverage better than other techniques (see section 2).
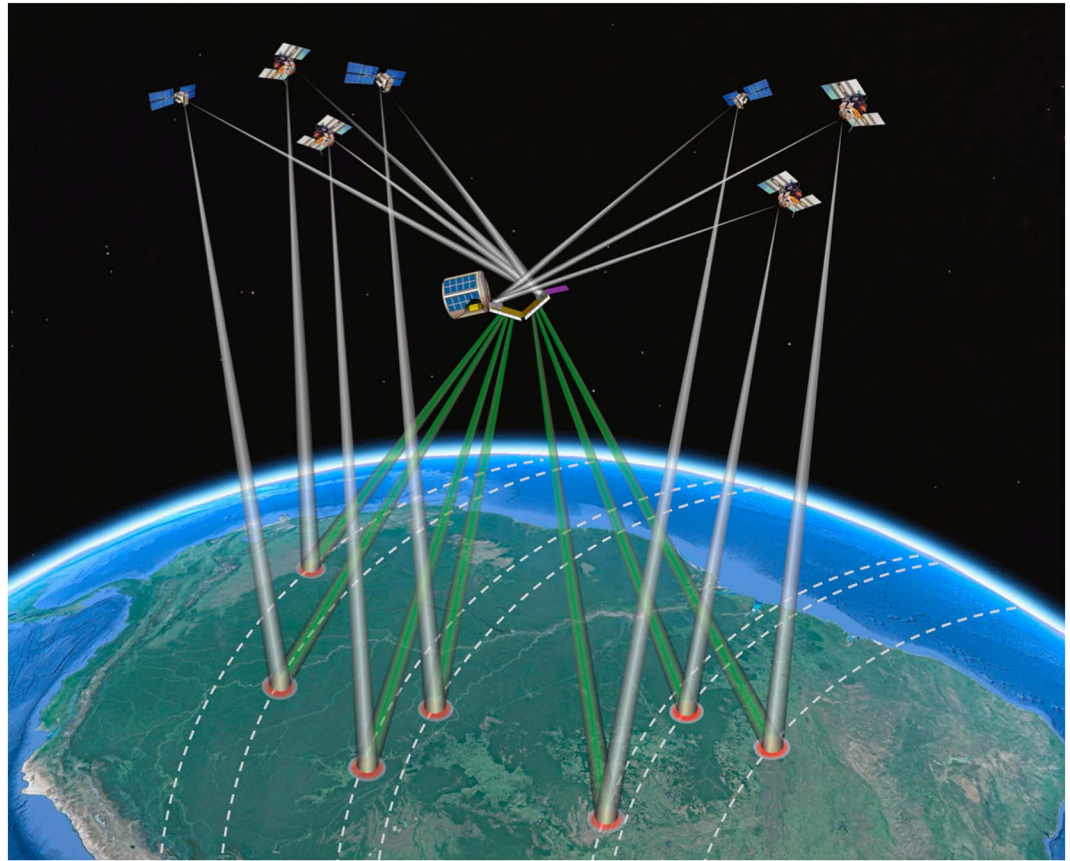
Figure 3. Geometry of GNSS-R showing a receiver in a low Earth orbit (LEO) collecting specular reflections from a constellation of GNSS transmitters. Received GNSS signals convey information of properties of reflecting surface. One receiver can measure signals from several transmitters reflected from the surface along several ground tracks (white dashed lines). As the satellite receiver flights along its orbit, the multiple tracks become long swaths on the Earth surface having swath width corresponding to the cross-track footprints determined by the Fresnel zone at each local segment.

The GNSS-R was first proposed by *Hall and Cordey* [1988]. GNSS signals reflected from the Earth's surface are used to measure surface properties such as ocean winds [*Ruf et al.*, 2016a; *Zavorotny and Voronovich*, 2000; *Garrison et al.*, 2002], sea ice coverage [*Fabra et al.*, 2011], soil moisture [*Chew et al.*, 2014, 2015b, 2016; *Camps et al.*, 2012, 2016; *Egido et al.*, 2014; *Katzberg et al.*, 2006; *Rodriguez-Alvarez et al.*, 2009; *Small et al.*, 2016], and potentially mean sea slope and topography [*Clarizia et al.*, 2016; *Cardellach et al.*, 2014a]. Soil moisture can impact the Bowen ratio and thereby affects tropospheric water vapor profile (measurable with GNSS Radio Occultation or RO) and changes atmospheric dynamic patterns. These in turn drive the transport of CH_4 emission from wetlands. In addition, the GNSS-R capability to estimate biomass has been demonstrated with aircraft measurement [*Egido et al.*, 2014], which circumvents the signature saturation issue in radar backscatter causing a significant underestimation of biomass retrieved from backscatter data [*Mermoz et al.*, 2015; *Egido et al.*, 2014; *Ferrazzoli et al.*, 2011]. With an optimal design, a GNSS-R/RO constellation can provide interconnected observations of atmospheric humidity, soil moisture change, and evolving wetlands extent.

For GNSS-R, the receiver with a downlooking antenna collects scattering contributions in the forward scattering direction (Figure 3) from an area around the specular reflection point, determined by delay and Doppler filters designed to effectuate a surface selectivity by a coherent integration in the receiver. By cross correlating the transmitted signal along the propagation path, a sequence of coherently integrated reflection waveforms is generated. These are subsequently summed incoherently, over selectable intervals yielding a series of independent reflection measurements. This bistatic radar concept takes advantage of the ever increasing number of GNSS transmitting satellites, and yields many randomly distributed measurements with broad-area global coverage and rapid revisit times.

Most GNSS-R measurements are either altimetric or scatterometric. GNSS-R altimetry, first described by *Martín-Neira* [1993], uses the difference in arrival time (delay) between the direct and reflected signals (obtained by either cross correlation with a model of the transmitted signal or cross correlation with direct signals) to measure the surface height relative to the receiver. Sufficiently precise altimetric performances would require an appropriate system design, such as in GEROS-ISS as a dedicated altimetric GNSS-R mission [*Wickert et al.*, 2016]. This method, combined with the knowledge of the receiver location deduced from GPS precise orbit determination, gives measurements of the ocean surface topography [*Lowe et al.*, 2002; *Hajj and Zuffada*, 2003; *Rius et al.*, 2010; *Cardellach et al.*, 2014a]. Mapping mesoscale ocean eddies, tsunami detection, and sea ice free board are examples of possible science measurements using GNSS-R altimetry. Potentially relevant to wetland mapping is GNSS-R scatterometry [*Garrison and Katzberg*, 2000], which uses features of the returned signal pulse shape such as peak power, rise time, or trailing edge to derive geophysical properties on land and water surfaces.

The cross-correlation process used to acquire a GNSS-R measurement corresponds to an integration of scattering contributions from a portion of the surface around the specular reflection point [*Zavorotny and Voronovich*, 2000], whose extent is determined by the type of scattering (incoherent or coherent), receiver location, the reflection geometry, the bandwidth of the GNSS codes being cross correlated, and the actual cross-correlation algorithms. Additionally, individual measurements can be summed incoherently by the receiver to produce higher-SNR (signal-to-noise ratio) data products at a selected time interval (typically, 1 s). All of these factors affect the measurement resolution. In general, the forward scattering contributions corresponding to the points on the surface having the same range describe ellipses whose semimajor and semiminor axes, *a* and *b*, respectively, are given by [*Hajj and Zuffada*, 2003]

$$a = \frac{1}{\sin\varepsilon}\left(\frac{R_r R_t \Lambda}{R_r + R_t}\right)^{1/2}, \quad b = \left(\frac{R_r R_t \Lambda}{R_r + R_t}\right)^{1/2} \tag{1}$$

where R_t is the distance between specular point and transmitter, R_r is the distance between receiver and specular point, ε is the reflection elevation angle, and Λ is the length of the GNSS code chip. For example, the GPS coarse/acquisition (C/A) code has a chip length of ~293 m, and the precision P(Y) code has a chip length of ~29 m. If the reflection is coherent, the majority of the cross-correlation output power comes from an area within the first Fresnel zone. In this case, equation (1) represents the size of the first Fresnel zone and Λ corresponds to the wavelength of the GNSS signal (for example, GPS L1 has a wavelength of ~19 cm). This is relevant since GNSS-R measurements over wetlands are predominantly coherent, with a potential spatial resolution ~1 km^2, depending on the geometry and satellite altitude.

Under the coherent reflection condition, theoretically, the magnitude of the reflected power is formulated by [*De Roo and Ulaby*, 1994; *Pierdicca et al.*, 2012]

$$P_{\text{coh,rl}} = \Gamma_{\text{rl}}\frac{P_t \lambda^2 G_t G_r}{(4\pi)^2 (R_t + R_r)^2} \approx \Gamma_{\text{rl}}\frac{P_t \lambda^2 G_t G_r}{(4\pi)^2 (R_t)^2} \tag{2}$$

where $P_t G_t$ is the equivalent isotropically radiated power (EIRP) of the transmitted signal (e.g., GPS L1 signal), G_r is the antenna gain of the receiver, and Γ_{rl} is the left-hand circularly polarized (LHCP) reflectivity of the reflecting surface at the observation geometry for GNSS-R. In the next section, this formulation will be used in the analysis of data acquired during an aircraft field campaign over the Ebro River Delta in Spain. In this case, the approximation in equation (2) uses the fact that $R_t \gg R_r$ at such aircraft platform height. On the other hand, for an incoherent reflection (which typically happens over the ocean), assuming a polarization and geometry-dependent bistatic scattering coefficient σ_0, the total scattered power is given by the bistatic radar equation [*Zavorotny and Voronovich*, 2000]

$$P_{\text{incoh}} = \frac{P_t \lambda^2}{(4\pi)^3}\int\frac{G_t G_r}{R_t^2 R_r^2}\sigma_0 \chi^2(\delta\tau, \delta f)\mathrm{d}A \tag{3}$$

where $\chi^2(\delta\tau, \delta f)$ is the Woodward Ambiguity Function of the GPS modulation code (e.g., GPS C/A code or P(Y) code) over a range of delay τ and range of Doppler frequency f.
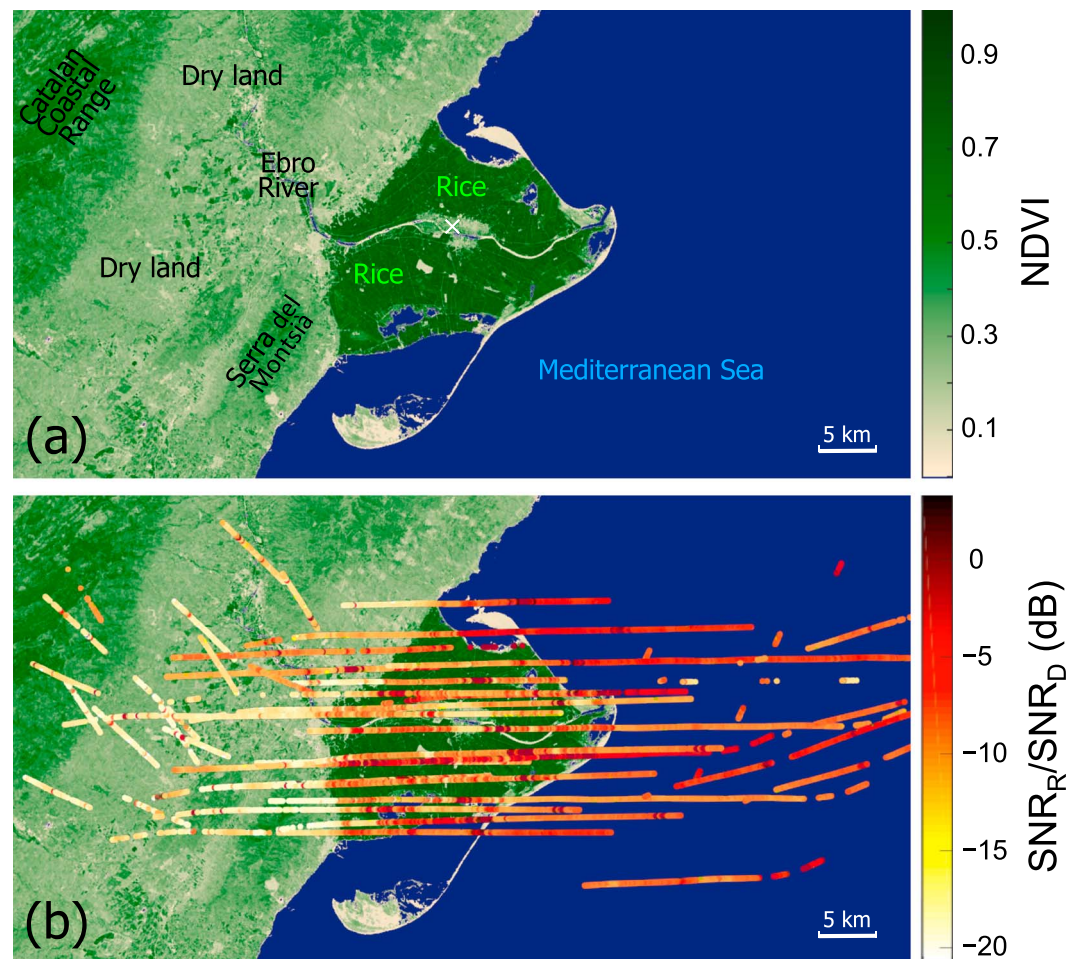
Figure 4. Measurements over the Ebro River Delta: (a) NDVI derived from Landsat satellite data on 14 July 2005 when the sky was mostly clear and (b) ratio of the SNR of the reflected waveform to the SNR of the direct waveform along the flight lines conducted on 13 July 2005 during the Catalonia flight campaign in Spain. Over land, distinctively higher SNR values are observed over the rice fields (darkest green areas) as compared to the values around the town of Deltebre marked by the white cross and over dry land (lighter green area). The size of each point (0.5 km) in the figure corresponds to the median size of area covered by coherent reflections (see equation (1)), typically occurred over the inundated rice fields. The actual size will vary due to coherency, geometry, and 1 s incoherent summation of the data. However, the incoherent summation does not have large effect on resolution from airborne instrument because the specular point does not travel a long distance in 1 s.

4. Wetland Results From the Catalonia Flight Campaign

4.1. Flight Campaign

A series of GNSS-R experiments using a reflectometry instrument for ocean measurement was carried out by Institut de Ciències de l'Espai (ICE-IEEC). Three test flights using a GPS Open Loop Differential Real-Time Receiver (GOLD-RTR) were conducted on 13–14 July 2005 [*Cardellach et al.*, 2011]. During these test flights, the aircraft was flown over rice fields on inundated land of the Catalonia wetland in the Ebro River Delta (Figure 4). Growing rapidly from sediment washed downriver, this delta is one of the largest wetland areas (320 km^2) in the western Mediterranean region [*Mañosa et al.*, 2001] and is on the Ramsar Convention list of wetlands of international importance [*Ramsar Convention*, 2015]. This region in northeastern Spain is mainly used for agricultural production of rice (main crop), citrus fruit, and vegetables, while a large part of the delta is designated as a Natural Park rich in wildlife. During July, when the test flights were held, the rice fields in the Ebro River Delta were in the maturation stage. The inundated rice fields were covered by a dense rice canopy, as verified with the high value of the Normalized Difference Vegetation Index (NDVI) image of

the Ebro River Delta region (Figure 4a) observed by the Landsat Satellite on 14 July 2005 when the sky was mostly clear.

The elevation angle of all the reflected waveforms was between 30° and 70°. The aircraft attitude information collected during the flight campaign was used in selecting waveforms only from straight and level flights to maintain the consistency and accuracy of the measurements. The fixed uplooking and downlooking antennas had a maximum gain of 6.5 dBIc and an omnidirectional pattern in azimuth. The precise antenna elevation pattern was not recorded during the flight, which causes a difficulty in the estimation of the power because the antenna gain in the direction of the specular points varies during different parts of the flight due to the changing geometry at different locations. To overcome the limitation due to the lack of the antenna pattern information, the data from different terrains were only compared for bins where the elevation angles of the geometry were within a degree of each other, i.e., at the transition of the specular point from one terrain type to the adjacent one where the target direction remains similar.

Data from the GOLD-RTR test flights included direct and reflected delay waveforms that were produced using coherent integration of 1 ms and incoherent averaging of 1 s [*Cardellach et al.*, 2011]. This data set is used to carry out the analysis in section 4.2. However, for optimal resolution and power over various terrain types, the coherent integration time can potentially be extended to a few tens of milliseconds rather than 1 ms when the reflections are strongly coherent (e.g., over wetlands as shown in section 4.2) and the incoherent summation can be eliminated, thus improving the spatial resolution [*Hajj and Zuffada*, 2003].

4.2. Data Analysis

A detailed power analysis for the GOLD-RTR test airborne experiment was conducted over various terrains including rice fields, forests, city, mountain, lake, and ocean. Each specular reflection point was classified into various terrain types: ocean, rice field, lake, river, dry land, city, and mountain. Digital elevation model (DEM) data and a water mask derived from *Shuttle Radar Topography Mission* [2014] were used to classify the reflection points from mountains, flat land, and ocean. Land cover-land use change data from *Institut Cartogràfic i Geològic de Catalunya* [2015] were used to further classify flat land data into different terrain types: lake, rice field, river, city, and dry land.

The waveforms from each type are shown in Figure 5. The results reveal that the waveforms from the rice fields and lake are mostly triangular in shape, an indication that the reflections from these surfaces are primarily coherent. In contrast, the reflected waveforms from ocean surfaces have mostly rounded peaks and are widened on the trailing edge, an indication that the reflections from ocean are primarily incoherent [*Hajj and Zuffada*, 2003]. Furthermore, the reflected waveforms from mountains are noisy (Figure 5, bottom right) and those from dry flat land and city have very low power levels. The reflected waveforms from mountains are noisy because the waveforms are transects of Delay-Doppler Maps (DDMs) at the specular point along the delay axis at the central value of the Doppler frequency. The specular point for these waveforms is computed from the geometry based on an ellipsoidal Earth. When the terrain deviates significantly from this assumption, which is the case for mountains, the peak of the waveform is outside the lag window within which the data are saved, and hence the resultant is mostly noise. These observations suggest that the potential use of GNSS-R scatterometry to detect wetlands should utilize both the coherency and the high power level of the signatures.

The average SNR was computed for data from each terrain class. The SNR was obtained by taking the peak value after subtracting the noise floor and dividing it by the noise floor, defined by the waveform values before the leading edge starts. The reflected SNR_R was then divided by the direct SNR_D to remove variations in the power caused by changes in the direct signal power. The spatial pattern of the ratio SNR_R/SNR_D along the level flight tracks over the study domain is presented in Figure 4b. These flight tracks were obtained on 13 July 2005, just one day earlier than the NDVI observations (Figure 4) from available Landsat data, which indicate how green the area was during the Ebro flight campaign. Although Figure 4b suggests some differences observable between dry land and wetlands, a prudent quantitative analysis is necessary to account for antenna gain effects.

The mean and median of SNR_R/SNR_D over each terrain class are summarized in Table 1. The highest median value of SNR_R/SNR_D is from the open-water lake, which is 2.97 dB higher than that from the rice fields. The SNR_R/SNR_D median value from the ocean is 1.3 dB higher than that from the rice fields and 1.67 dB lower than
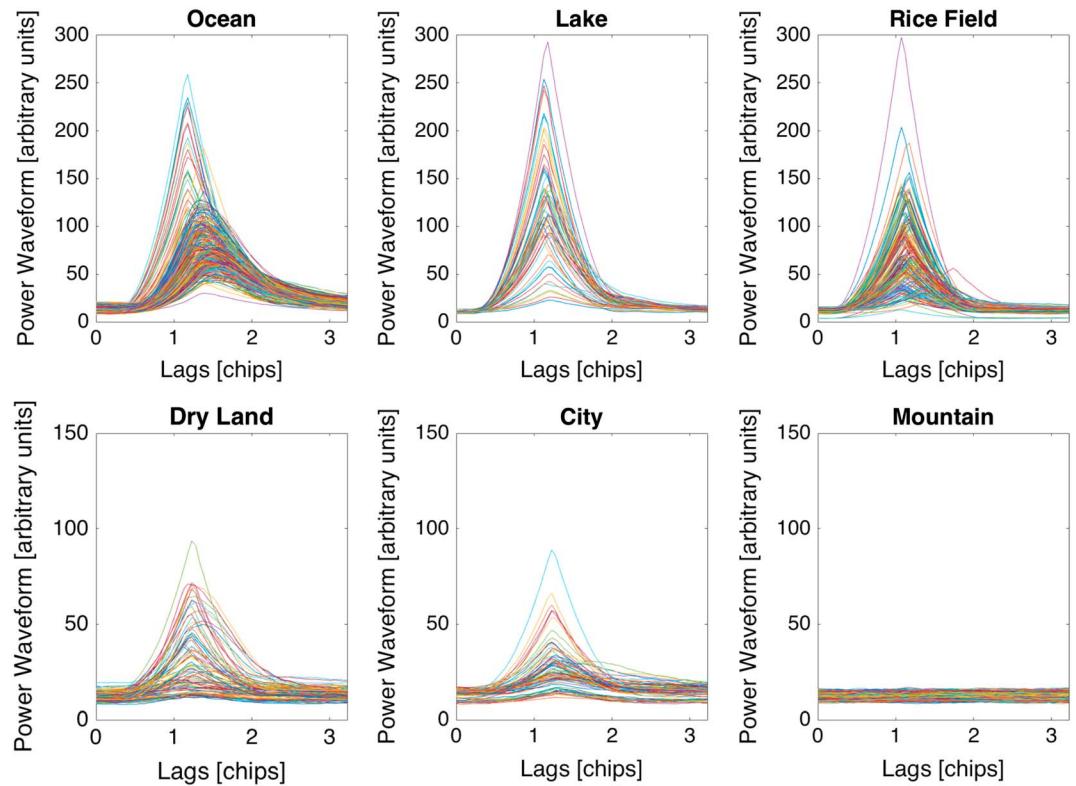
Figure 5. Waveforms of reflected power measured for various terrain classes from a representative ensemble of waveforms for each terrain class. On the top row are example waveforms from (right) rice fields, (middle) lake, and (left) ocean. On the bottom row are example waveforms from (right) mountains, (middle) city, and (left) dry land. Note the different vertical scales.

that from the lake. These are consistent with results in Figure 5, showing the highest reflected power being from lake followed by ocean and rice fields. The median values between terrains, given in Table 1, should not be compared directly due to the unknown antenna gain pattern at different GNSS-R measurement geometry. To address this difficulty, a method needs to be developed to compensate for the antenna gain pattern and thereby allow a consistent comparison of SNR ratio between different terrains. This is done by binning the values of SNR by 1° elevation angle and computing the median for each terrain for each given elevation angle bin. The difference between any two terrain types is computed only within the same bin of elevation angle (if the data are present for both terrain types for a given bin) and the summary of the differences is shown in Table 2.

This relative comparison between data of the same elevation angle can account for the unknown antenna gain pattern as explained below. First, because the omnidirectional antenna has an azimuthal gain symmetry, it is independent of the azimuth angle ϕ so that $G_D(\theta, \phi) = G_D(\theta)$ and $G_R(\theta, \phi) = G_R(\theta)$, where G_D is the gain of the uplooking receiver antenna and G_R is the gain of the downlooking receiver antenna, θ is the elevation angle for both the direct and reflected signals. Then, at a given time t, the ratio of SNR is $SNR_R(\theta, t)/SNR_D(\theta, t)$. The two antennas are similar (NovAtel Model 512) and the data points considered in this analysis were

Table 1. Mean and Median SNR_R/SNR_D Computed in Decibel (dB) for Various Surface Classes in the Study Domain of the Catalonia Flight Campaign in Spain

Terrain Type	SNR_R/SNR_D (dB)		
	Mean	Median	Standard Deviation
Ocean	−9.58	−10.06	1.28
Lake	−8.01	−8.39	1.87
Rice field	−10.86	−11.36	2.25
Dry flat land	−15.73	−16.30	1.38
City	−14.67	−14.48	1.78
Mountain	−17.62	−17.91	0.75

Table 2. Mean and Median SNR_R/SNR_D Difference Computed in Decibel (dB), Using the 1° Elevation Angle Binning Method, for Various Surface Classes When Compared to Rice Field in the Study Domain of the Catalonia Flight Campaign in Spain

|	Difference in SNR_R/SNR_D (dB)		
Terrain Type	Mean	Median	Standard Deviation
Rice field-lake	−2.63	−2.45	2.04
Rice field-ocean	−1.53	−1.54	1.70
Rice field-dry flat land	4.16	3.61	2.68
Rice field-city	2.56	2.24′	2.66
Rice field-mountain	6.79	6.79	3.48

from when the airplane attitude was straight and level, which made the angle for uplooking and downlooking antennas similar.

Before obtaining the results in Table 2, we compared data between two adjacent terrains where the specular reflection point moved from one type of terrain to another. Since we looked at two adjacent terrain types during the short time duration for this comparison, the elevation angle remained virtually constant. We then compared that result with all the data points within 1° elevation angle but with varying azimuth (i.e., the result in Table 2) at different times. These two results were found to be very similar, thereby verifying the azimuthal symmetry of the antenna gain pattern for data within the same incidence angle bin. This is because the absolute level of the power from the unknown antenna pattern is canceled out in the pair ratio of the power ratios of two different surface types, given by $[SNR_{R1}(\theta, t)/SNR_{D1}(\theta, t)]/[SNR_{R2}(\theta, t)/SNR_{D2}(\theta, t)]$, where subscripts 1 and 2 denote surface types 1 and 2, respectively. The gain cancelation occurs in the pair ratio because the antenna gains (in equation (2)) are approximately the same within each 1° bin of θ and remain stable with time t as confirmed by the test explained above. As demonstrated by this analysis, the GNSS-R pair ratio method offers an advantage, as it is robust to variations in the antenna pattern in the development of an optimal algorithm for wetland detection using GNSS-R signatures.

After accounting for the unknown antenna gain pattern in the ratio method, the power return from rice fields was found to be 2.37 dB lower than that from the lake, and 1.35 dB lower than that from the ocean, both of which are open-water surfaces that can be identified and mapped by synthetic aperture radars [*Santoro et al.*, 2015; *Brisco et al.*, 2009; *Slater et al.*, 2006]. More importantly, the return from rice fields was 3.68 dB higher than from dry flat land and 2.61 dB higher than from a city. This result demonstrates that the power of the GNSS-R signals over the wetland is almost as much as the power of the reflections over the ocean surface while that over the dry land is sharply lower. During July (Figure 6), the difference between the power from ocean/lake and the peak growth rice fields can be partly attributed to the signal attenuation through the

Figure 6. Rice plants at peak growth on inundated land in the area of Mas de La Llanada of the Catalonia wetland in the Ebro River Delta. This rice field is located about 3 km south of the village Sant Jaume d'Enveja. Photo credit to M. Cebolla/Archives of the Natural Park of the Ebro River Delta (PNDE).
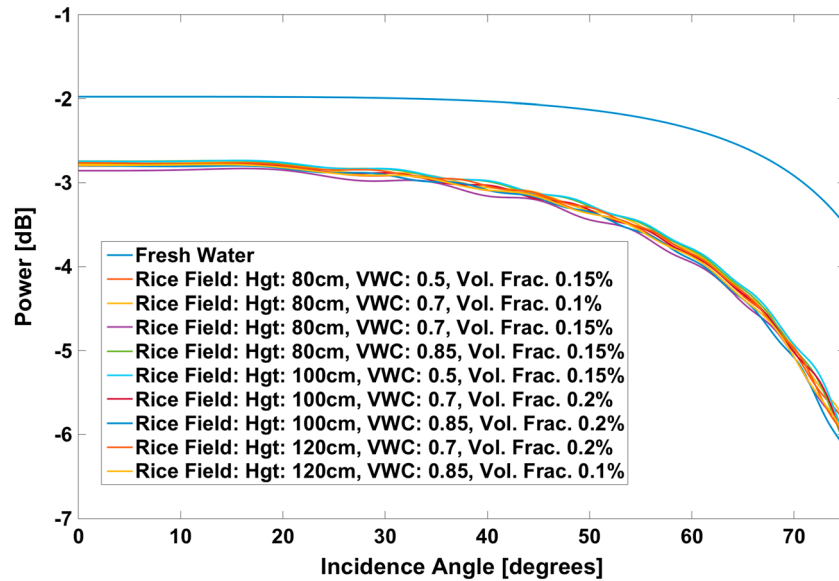
Figure 7. Power return from a rice field with a rice canopy over inundated soil, using modeled reflectivity of lake and rice fields for variable wetland parameters.

dense rice canopy. Despite the vegetation attenuation, the strong forward reflection from the smooth water surface on the inundated rice fields allows a distinctive identification of wetlands from the dry land.

4.3. Model Analyses

Measurements indicate that the waveform shapes from lake and rice fields are more coherent than those from the Mediterranean Sea surface that are only partially coherent (Figure 5). The peak power return from the rice fields is essentially the coherent return from the water surface on the inundated land attenuated by the overlying rice canopy. Under this coherence condition, the formulation of the radar equation given by (2) is used for a model analysis of the GNSS-R signal. Because there was no dedicated surface campaign to collect in situ field data at the time of the experiment, the simulations below are intended to convey only the general response of the signal to typical mature rice crops and whether or not the observed power returns are reasonable.

The reflectivity values for fresh water and rice fields were computed using reflection coefficients generated from a layered dielectric model described in the published literature [*Chew et al.*, 2015a]. The one-dimensional, single-scattering forward model calculates reflection coefficients at a given polarization, signal frequency, and angle of incidence, using the small perturbation method outlined in *Fuks and Voronovich* [2000]. The model uses inputs of soil moisture and texture parameters, from which a dielectric profile is determined using values from *Hallikainen et al.* [1985]. Here we set the complex dielectric constant of the bottom model layer to $\varepsilon_w = 77.59 + i\, 6.86$, which represents fresh water at a temperature of 25°C at the GPS L1 frequency (1575.425 GHz), obtained by interpolating values from *Kaatze* [1989].

The dielectric slab above the water surface was either set to the dielectric constant of air ($\varepsilon_{air} = 1.0$) for the case of bare freshwater surface or to represent the effective dielectric constants of rice fields at varying stages of growth. Dielectric constants of the vegetation were determined using the semiempirical model presented in *Ulaby and El-Rayes* [1987] and the complex refractive index mixture equation by *Nelson* [1991]. Different power curves were generated by varying the conditions of rice fields over different vegetation water content, salinity, rice plant volume percentage, and rice plant height as listed in the legend of Figure 7. The power curves that best matched the experimental result are plotted in Figure 7.

Since the GPS transmits a right-hand circularly polarized (RHCP) signal, the forward scattered coherent reflected signal is primarily LHCP for the range of elevation angles from this experiment. By inserting the calculated reflectivity values and keeping the other parameters the same in equation (2) between lake and rice fields, the power levels closest to the measured values (as summarized in Table 2) is found in the range of rice

canopy heights of about 80–120 cm (belly to chest height of the farmers as a reference in Figure 6), which is consistent to a typical mature rice crop at the peak growth stage in July. Nevertheless, different vegetation conditions and water surface roughness can affect the power level of the reflected signal.

5. Wetland Observations From TechDemoSat-1 (TDS-1) Satellite

TDS-1 is a small satellite mission for technology demonstration privately funded by Surrey Satellites Technology Ltd (SSTL) in the United Kingdom (UK) [*Surrey*, 2015]. TDS-1 was launched in July 2014 in a Sun-synchronous orbit at an altitude of ~635 km around the Earth. TDS-1 is derived from a heritage technology, which functions as an in-orbit test facility for innovative UK payloads and software [*Foti et al.*, 2015]. One of the eight payloads is the Space GNSS Receiver Remote Sensing Instrument (SGR-ReSI) developed by SSTL. The SGR-ReSI collects GPS signals reflected off the Earth's surface and processes them into DDMs of power as a function of time (delay) and Doppler frequency (delay resolution of 250 ns and Doppler resolution of 500 Hz).

The peak amplitude and the behavior of the trailing edge of the DDM give information about the surface roughness and dielectric properties at the specular reflection point, from which relevant geophysical parameters can be derived. A subset of TDS-1 data, collected over a 6 month period ending in June 2015, has been made available to the public [*Measurement of Earth Reflected Radio-navigation Signals by Satellite*, 2015]. Examples of 1 s incoherently averaged DDMs have been published [*Chew et al.*, 2016], where power waveforms discussed in section 4 correspond to cuts of the DDM along the delay axis at the central value of the Doppler frequency [see *Chew et al.*, 2016, Figure 1]. Note that the SGR-ReSI will also be flown on CYGNSS (see section 6.1) with minimal design changes.

Available TDS-1 Level-1B (L1B) data acquired over wetlands are analyzed to assess the potential use of satellite GNSS-R data for wetland mapping. As the gain pattern of the TDS-1 antenna is known, the computed power is corrected for antenna gain, receiver range, and elevation angle. Here we report values of reflected power with respect to the computed power for DDMs that do not contain a clear reflection/no distinction in peak power, such that a value of 10 dB would indicate a 10 dB difference between the peak power and the noise value.

The power analysis of TDS-1 DDM peaks over the Ebro River Delta shows that the power from the wetland (rice fields) is distinctively larger than that of the adjacent dry land, specifically by as much as 10 dB (Figure 8). At the time of the TDS-1 overpass (5 February 2015), much of the Ebro River Delta was devoid of rice and mostly covered by shallow water and mudflat with water [*Moré et al.*, 2011] as seen in Figure 9. Such surface condition is also confirmed in a multispectral false-color Landsat-8 image (Figure 8b). The highest reflected power is observed over the Ebro River. Two other areas of reflected power, immediately north and south of the river, were likely high due to water underlying an area with agricultural activity in February (bright green area north of Ebro River) and standing water on fallow fields (indicated by the blue patches of water south of the river).

There is a significant increase in reflected power (shown in red) from the rice fields compared to that over the surrounding ocean (Figure 8). This is in contrast to what was observed during the aircraft campaign shown in Figure 4. During the aircraft campaign, higher reflected power was observed over the ocean with respect to the land surface. There are several possible reasons why observations from space would differ from those observed from the aircraft: (a) the contribution area from aircraft is smaller, (b) the elevation angle of the reflection geometry from aircraft is larger, (c) the large glistening zone from space includes more inhomogeneity over the rough ocean surface, (d) wind and wave conditions are different in the two cases, or (e) combinations of (a)–(d). In either case, land and ocean surface can be identified readily with existing topographic or bathymetric data sets [*Weatherall et al.*, 2015]. Here the key result is the distinctive difference in GNSS-R signatures between wetland and dry land (>4 dB), allowing their identification as demonstrated in both aircraft and satellite observations. Nevertheless, the TDS-1 data are only available in 1 s incoherently averaged values, causing the TDS-1 footprint to be elongated or smeared along the ground track (Figure 8b), which is not optimal for wetland mapping.

TDS-1 data are also available over the Mississippi basin, which is the same region as in Figure 1. There are two TDS-1 tracks crossing extensively over the Mississippi River and adjacent watersheds (Figure 10a). Overall,
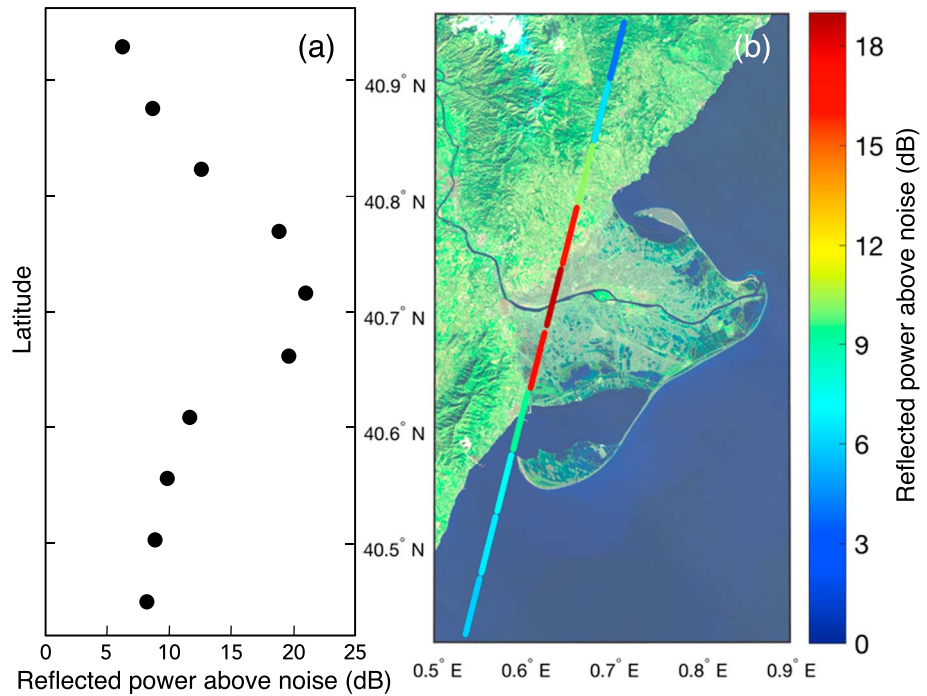
Figure 8. Power analysis of 1 s averaged TDS-1 DDM peaks on 5 February 2015 over the Ebro River Delta: (a) Point-wise plot of the reflected power above noise and (b) map of the reflected power above noise overlaid on a false color (bands 7, 5, and 3) from Landsat 8 on 8 February 2015 with green areas indicating significant vegetation growth and blues areas for open or standing water. On the map (Figure 8b), the along-track ellipses are 7 km long because of the 1 s averaging and the distance that the spacecraft travels in this 1 s. It is noted that the size of each point in the cross-track direction in the figure corresponds to the median size of the area sampled by coherent reflections (see equation (1)), typically occurring over the inundated rice fields (0.5 km). The actual size over ocean or dry land will vary due to coherency and geometry.

TDS-1 reflected power is generally elevated over the Mississippi basin (yellow areas in Figure 10a), corresponding to the region where wetland extent was detected by QuikSCAT and MODIS (Figure 1). Although the TDS-1 power data are corrected for antenna gain, receiver range, and elevation angle, data from direct GPS signals are not available. Consequently, the reflected power might have variability due to changes in

Figure 9. In winter, there is no rice plant over the Catalonia wetland in the Ebro River Delta, but rather it is mostly covered by shallow water and mudflat with water as seen in this photograph taken at 40.729°N and 0.634°E. Photo credit to Google.
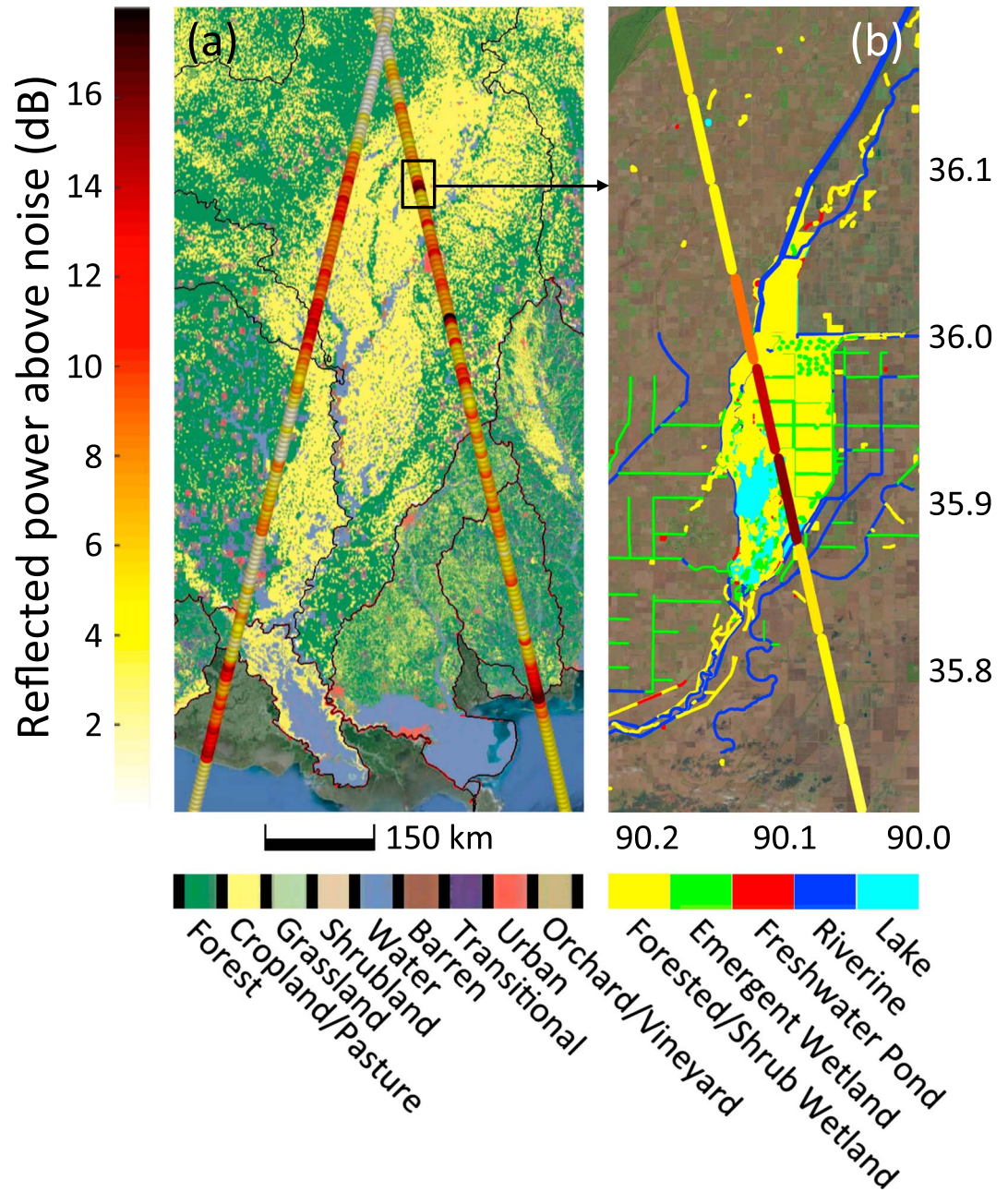
Figure 10. TDS-1 satellite signatures along the west track acquired on 15 November 2014 and the east track on 20 February 2015: (a) over the Mississippi and adjacent watersheds marked with the black boundaries overlaid on land cover from the National Land Cover Database [*USGS*, 2016] and (b) over the Big Lake Wildlife Refuge and adjacent areas, given by the north latitudes and west longitudes in degrees, together with wetland data from the National Wetlands Inventory [*FWS*, 2016b]. The vertical color bar, applicable to TDS-1 GNSS-R data in both Figures 10a and 10b, represents normalized reflected power defined as the difference in decibel between the reflected power from a given location and the overall reflected power averaged over all land during the entire TDS-1 satellite data collection period from September 2014 to February 2015.

the transmitted signal along a long ground track or along different ground tracks. Unless the difference in the reflected signature is very strong, detailed and subtle patterns of the reflected power along long and/or different paths need to be interpreted with care.

To account for the lack of data from direct GPS signals, a short ground segment in a given ground track should be used to avoid inconsistent effects from the variability in the direct signals. This is because the direct

Figure 11. Vegetation cover over wetland in the Big Lake National Wildlife Refuge. On the forested wetland, the water surface is mirror-like causing strong coherent reflection of GNSS signal. The tree canopy and floating vegetation can obscure optical signatures. Tall trees may saturate monostatic radar backscatter signatures. In these cases, GNSS-R can identify the inundated wetlands (see Figure 10b). This photograph was taken at 35.855°N, 90.136°W. Photo credit to Steven Rimer, Refuge Manager, Big Lake National Wildlife Refuge.

signals should be from the same GPS transmitter that remains stable over the short time along the short segment. This is the approach used in the case of the Ebro River Delta where the TDS-1 track spanned over a short distance across the rice fields. This method is used again here to demonstrate the capability of satellite GNSS-R to detect inundated wetlands under a thick vegetation cover. In this case, a segment of the TDS-1 ground track passing across a heavily vegetated wetland area near the town of Manila in Mississippi County, Arkansas, is examined (Figure 10b). This area includes the Big Lake National Wildlife Refuge [*Fish and Wildlife Service* (*FWS*), 2016a] together with the Hornersville Swamp Conservation Area on the north and the Big Lake Wildlife Management Area on the east. Created by the New Madrid Earthquakes of 1811–1812, the Big Lakes refuge consists of bottomland hardwood forest, wooded swampland, and open water [*Bennett*, 2016].

Over the forested and shrub wetlands under tall trees and thick understories (Figure 11) in the Big Lake refuge and adjacent areas, the TDS-1 reflected power was distinctively higher over the wetland compared to that over the adjacent cropland (Figure 10b and Table 3). Quantitatively, the average reflected power from the wetland (orange-red elongated footprints, Figure 10b) is found to be 9.85 dB higher than the average power from the adjacent land (yellow elongated footprints, Figure 10b). This represents an equivalence of

Table 3. Mean and Median Reflected Power Over Noise Computed in Decibel (dB) for Various Surface Classes in TDS-1 Data Over Mississippi Delta

Terrain Type	Reflected Power over Noise (dB)	
	Mean	Median
Lake	16.03	17.29
Estuary	9.97	9.92
River/Floodplain	9.72	9.19
City	7.36	8.25
Forest	6.31	6.42
Farmland	5.31	5.3
Ocean	5.4	5.28

9.7 times stronger for the GNSS-R wetland signature and thus the GNSS-R satellite measurement can identify forested wetlands even under the thick vegetation cover as demonstrated in this case.

A constraint to TDS-1 satellite data is the elongated footprint size of the reflections over wetlands (which are primarily coherent), which is <1 km offtrack and smeared to 7 km along track. The coarse along-track resolution is primarily because the DDMs are averaged over 1 s. This 1 s averaging is, however, not necessary and not desirable for coherent reflections. So the resolution could be improved in future missions by using shorter averaging intervals or just using coherent integration. On the other hand, the resolution of reflections over ocean (which are primarily incoherent) is about 25 km offtrack and 25 km along track, since the area of collection is a glistening zone defined by the chip length of the GPS C/A code. Thus, averaging time interval is clearly an important factor to be considered in designing a satellite GNSS-R system for remote sensing of wetlands. On a future mission, the direct signal can also be used to cross correlate the reflected signal as an interferometric technique. This will enable the use of wider bandwidth signals, which can further improve the accuracy and resolution.

6. Future GNSS-R Satellite Capabilities

6.1. The CYGNSS Mission

As a part of the NASA Earth System Science Pathfinder (ESSP) Program, the CYGNSS Venture-class mission will use a constellation of eight small satellites carried to orbit on a single launch vehicle [*Cyclone Global Navigation Satellite System*, 2015] to measure GNSS-R signals for retrieval of ocean wind speed. CYGNSS data will be useful to investigate GNSS-R signatures of wetlands through multiple timescales of wetland dynamics over the spatial coverage of CYGNSS, primarily in the tropics.

Beginning in Spring 2017, the CYGNSS mission is planned to deliver L1 DDM data (delay resolution 250 ns and Doppler resolution 500 Hz) including measurements over land. The L1A data product is DDMs of received power and the L1B product is DDMs of unnormalized scattering cross section (USCS). Also to be provided is an L1B ancillary product that is DDMs of effective scattering area (ESA) [*Ruf et al.*, 2016b]. That way, the end user can select a portion of the DDMs, divide USCS by ESA, and create a custom bin-averaged value (σ_0 in equation (3)). This is necessary because one cannot average across bins of a DDM of σ_0 and maintain calibration [*Ruf et al.*, 2016b].

The CYGNSS data has a nominal spatial resolution of 25 km × 25 km (centered on the specular reflection point). However, the native resolution is better than 25 km × 25 km. The resolution depends on the location of the specular point (better resolution nearer to subsatellite point at nadir). CYGNSS averages multiple DDM bins together to get to the 25 km × 25 km size for the baseline L2 wind speed data product, but this is not optimal for wetland mapping. However, the L1B data products can be exploited to optimize resolution over wetlands to higher value (e.g., <1 km × 7 km) similar to the TDS-1 analysis done in this paper. This is possible because the reflection from wetlands is coherent, and thus the active scattering area is defined by the first Fresnel zone. If the reflection were incoherent, then the resolution would be limited by the first chip. It is also desirable that experimental data products with a better spatial resolution be available to further investigate the capability of GNSS-R for wetland mapping.

The analysis for wetland identification from aircraft experiments and from TDS-1 satellite data can be adapted for use with CYGNSS satellite sensors. The peak power of the waveform from satellite sensors will be lower than that from the aircraft sensor so a corresponding algorithm to detect wetland will be adjusted to the new range of power return. The waveform shape analysis will still be valid to classify the reflection as coherent or incoherent, and the full DDM will be exploited for an optimal resolution computation. The methodology described in *Hajj and Zuffada* [2003], which uses DDM and spacecraft velocity direction along with antenna viewing angle, can be implemented to compute the footprint size. Additionally, since one of the L1B products from CYGNSS is the scattering cross section, this information will be applicable to assess vegetation cover over wetlands.

CYGNSS orbit inclination is 35°, resulting in a latitudinal coverage of about ±38.5°. The calculated revisit time has a mean of ~6 h, which is ample to investigate wetland dynamics in the tropics to midlatitudes. In particular, CYGNSS is optimized to provide a high temporal resolution to capture even short-term processes, particularly the generation, intensification, and decay of a tropical cyclone. This capability for frequent

observations with the high temporal resolution will enable observations of the wetland dynamics across a wide range of timescales. However, the latitude and resolution limitations of CYGNSS necessitates a synergistic approach for a global coverage from multiple GNSS-R instruments (next section) and from other satellite methods (section 2) to achieve a more complete dynamic mapping of global wetlands across different spatial and temporal scales.

6.2. Other GNSS-R Satellite Configurations

Two other spaceborne GNSS-R experiments are being prepared: the 3Cat-2 [*Carreño-Luengo et al.*, 2013] and GEROS-ISS. The 3Cat-2 is a six-unit cubesat developed by the Universitat Politécnica de Catalunya (UPC) and partially funded by the European grant FP7 E-GEM. It was launched on 15 August 2016 from the Jiuquan Satellite Launch Center in the Gobi desert. Unlike any previous spaceborne GNSS-R payload, it includes polarimetric features and precise altimetric capabilities. The GEROS-ISS is a mission under development by the European Space Agency, to install an innovative GNSS-R payload aboard the International Space Station. GEROS-ISS will perform altimetry using an interferometric GNSS-R technique, together with scatterometric GNSS-R measurements and Radio Occultation. The antenna gain is higher than for any previous dedicated spaceborne GNSS-R experiment, and it also has the possibility to take all these measurement at two polarizations (RHCP and LHCP), for both uplooking and downlooking antennas. The setup may extend the scientific possibilities for wetland monitoring and its link to the hydrological cycle. For example, the possibility to measure water level in wetland areas would complement the observations about flooding extension.

Furthermore, GNSS systems are not limited to the ~30 GPS transmitters but also include the ~24 satellite GLONASS system from Russia, plus the expected 30 satellites from Europe's Galileo system, 30 satellites from China's Beidou system, 7 satellites from India's IRNSS system, and 4 satellites from Japan's QZSS system. All of the constellations operate at L band (IRNSS also transmits at the S band frequency of 2492.028 MHz) and have satellites operating in medium Earth orbits. The availability of additional signal sources has been driving the design of receivers that can acquire all the available signals, a capability already demonstrated without adding excessive complexity to the instrument design. This opens the possibility of significantly increasing the density of the potentially available reflections.

In parallel, the optimal exploitation of measurements through GNSS-R systems requires constellations of receiving instruments, consisting of user-designed receivers and downlooking antennas with suitable characteristics for the type of observations intended (wetlands have different requirements from, say, ocean winds). Although currently not intended to be a GNSS-R constellation, the COSMIC 2 constellation could potentially offer such opportunity. Specifically, COSMIC 2, a joint Taiwan-US mission for the study of meteorology, ionosphere, and climate, has an option for six satellites deployed at high elevation (72°) to be launched near the end of this decade. Such a configuration could extend the reflection coverage to the higher latitudes, overcoming one of CYGNSS's limitations, thus providing a good synergy for global wetlands mapping and dynamics monitoring. An illustration of the hypothetical reflection distributions for COSMIC 2 is shown in Figure 12. Currently, there is no plan to add GNSS-R to COSMIC 2, while the planned GNSS receivers delivered for the primary mission goals could be readily modified to provide such capability with a modest incremental cost.

In addition to the L band navigation signals, there are other signals of opportunity (SoOp), whose primary purpose is digital satellite communication. These can be used as transmitters to create the same bistatic configuration as GNSS-R for wetland mapping. There are over 400 potential digital communication satellites that can be used as sources for SoOp (most of these satellites have emerged in the last decade). These signals range from P band to Ka band and a user-designed receiver can produce reflection waveforms by cross correlations of a direct signal with the reflected signal [*Shah et al.*, 2012; *Ribó et al.*, 2014]. Some of the features of these signals are as follows: (1) they are typically transmitted at power levels higher than those for navigation signals, (2) the majority of the transmitters are located at geostationary orbits which simplify geometry but affect temporal revisit time and resolution, and (3) the signals are distributed in a wide frequency range. More research is needed to determine if there is a combination of frequencies for wetland mapping and dynamics monitoring together with L band, where a good potential has already been shown.
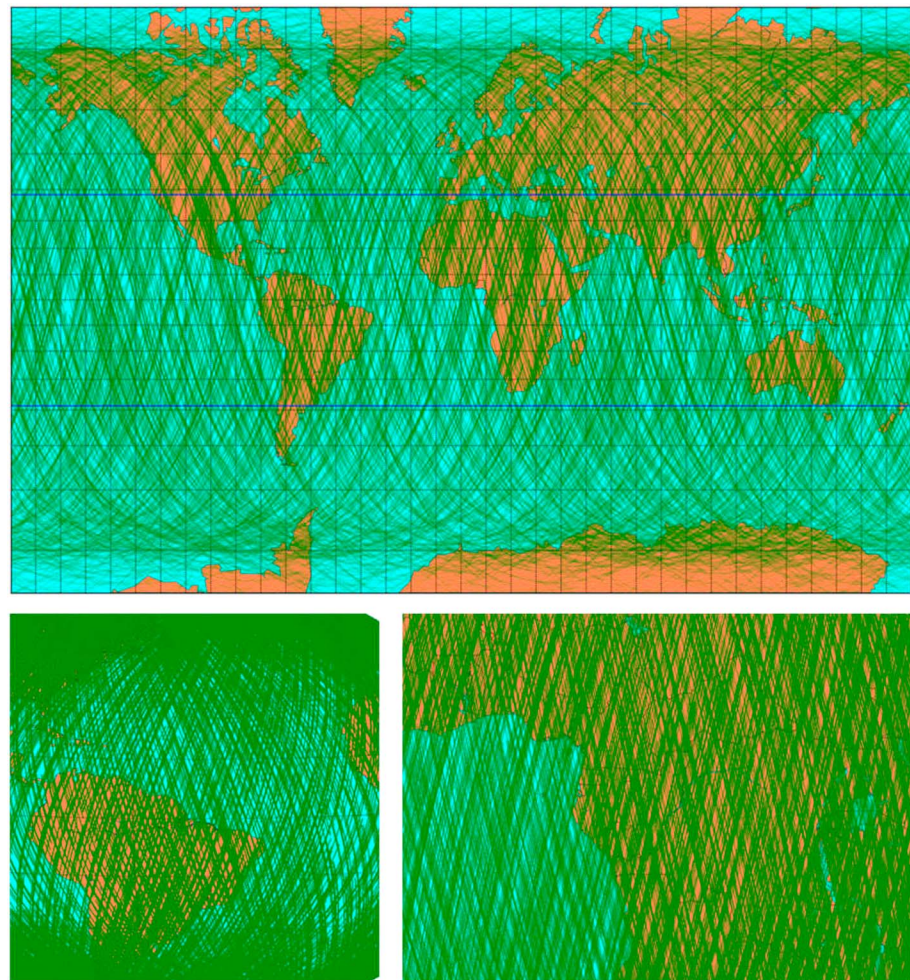
Figure 12. Spatial coverage from a combination of reflections acquired by (top) COSMIC-2 from GPS and GLONASS in 1 day over the world with the blue lines indicating the north and south limits of the CYGNSS coverage, (bottom left) COSMIC-2 from GPS, GLONASS, and GALILEO in 2 days over several continents, and (bottom right) COSMIC-2 from GPS, GLONASS, and GALILEO in 10 days over central Africa.

6.3. GNSS-R Advantages, Constraints, and Multisensor Synergy

Given the possible synergy with multiple satellite sensors, GNSS-R using distinctive signatures of wetland to map wetlands in space and monitor their change in time may lead to new advances. The advantages contributed by GNSS-R include the following: (1) frequent and global coverage from many dozens of transmitting satellites in multiple constellations, (2) long-term GNSS transmitters to be continued into the far future, (3) small antennas for a large field of regard while the resolution is determined by the Fresnel zone rather than antenna size, (4) low-cost small-size receivers and compact antennas allowing the deployment of multiple science instruments in each launch, (5) more robust and reliable GNSS-R systems with many sensors in constellations compared to the single-satellite sensor approach, (6) low frequencies unaffected by clouds or rain, and (7) strong forward reflection/scattering signatures to cope with signal obscurity by thick and dense vegetation cover over inundated wetlands. To realize such advantages, a constellation of GNSS-R science instruments flying in low Earth orbit must be designed to ensure an adequate coverage and repeat frequency. An illustration of the possible scaling of coverage of a constellation is provided in Figure 13, showing how the number of GNSS-R measurement points in a given cell size of the Earth surface increases as a function of the number of satellites.

GNSS-R also has limitations. For example, the signals are collected as a series of locations along surface tracks rather than forming an instantaneous image and the spatial resolution may be limited for observing detailed features in small or discontinuous wetlands. Therefore, a synergistic combination of multiple
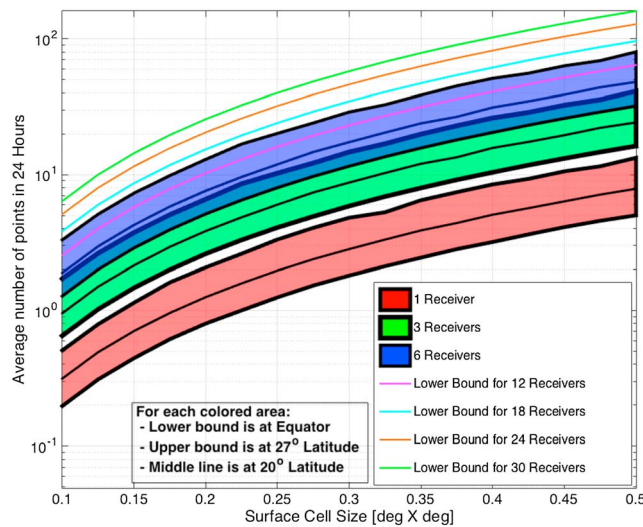
Figure 13. Number of reflection points (1 s average) in a given cell size on the Earth accrued in 24 h, as a function of the constellation size, assuming receivers at 24° inclination and altitude 700–800 km. Only reflections at incidence angles lower than 50° from normal are received, and it is assumed that all planned GPS/Galileo/GLONASS transmitters are active.

sensors is likely an optimal approach to cover a multitude of spatial and temporal scales of wetland dynamics. The synergy requires the use of the array of wetland products derived from active and passive remote sensing data in a multifold manner: (1) to compare and verify results from an initial GNSS-R wetland algorithm against different wetland detection results, (2) to improve GNSS-R algorithms together with the validity regimes of other methods, and (3) to identify what can be done and what may be missing from different methods in developing an optimal measurement strategy. For this purpose, community efforts need to be coordinated to develop an effective protocol for synergistic wetland mapping.

7. Discussions

7.1. Wetland Dynamics and Methane Emission

The development of an innovative synergistic GNSS-R wetland algorithm is expected to significantly contribute to providing observations of global wetland distribution and wetland dynamics. These are crucial toward filling the major missing gap of global wetland extent: (1) as a dynamic quantity required to understand the role of wetlands as drivers of CH_4 change, (2) to assess how these changes affect climate, (3) to address feedback consequences on wetland change, and (4) to improve projections of future CH_4 emission and water storage capacity and their impacts. The new GNSS-R-based capability potentially enables a breakthrough increase in the coverage and frequency of wetland observations across the world to capture timescales sufficient to allow new physical insights into various CH_4 pathways and potentially discover new processes that may be obscured by the lack of frequent global measurements.

Current knowledge of CH_4 pathways includes diffusion (CH_4 upward diffusion through soil and water), aerenchyma (CH_4 transport via tubes in plant tissues), and ebullition (CH_4 bubbling). A different science hypothesis that another pathway may exist is suggested by preliminary field observations of seasonal cycles of extreme releases, such as CH_4 roiling up from lakes or from wells (e.g., observed in wetland areas of Mekong Delta in Vĩnh Long, Vietnam [*VTV1*, 2012]). This different pathway is perhaps related to hydrostatic compression in subterranean CH_4 pockets by rising groundwater level from intensive rains or to subsurface transport flux in the aquifer with precipitation-induced changes in differential pressure gradient as governed by Darcy's law [*Whitaker*, 1986]. From this law, a model simulation suggests subsurface hydrologic pathways as mechanisms for CH_4 emission from groundwater-supported wetlands [*Miguez-Macho and Fan*, 2012]. These processes need to be identified and quantified; frequent and global measurements of wetlands advanced by the GNSS-R synergy can lead to reaching this goal. As the water cycle accelerates and intensifies in a changing climate [*Syed et al.*, 2010; *Durack et al.*, 2012], impacts on wetlands and CH_4 emission are expected. This issue necessitates a quantitative characterization of global wetland dynamics through multiple decades to sufficiently capture the climatic timescale.

7.2. Wetland Dynamics and Water and Energy Cycles

Within the global water and energy cycles, it is critical to identify and understand interrelations of hydrological cycles involving precipitation, soil moisture change, freeze/thaw state, inundation, stream flow, and runoff

together with wetlands dynamics and cycles of CH_4 emission change and water storage capacity change. Hydrologic alterations including wetland filling or drainage can impact water impoundment or release from continental drainage basins and significantly affect global sea level [*Gornitz et al.*, 1997; *Sahagian*, 2000].

A GNSS-R constellation that is also capable of radio occultation measurements could be part of a system for observing the global hydrological cycle. In particular, GNSS radio occultation (GNSS-RO), based on the refraction of GNSS signals passing through the atmosphere, has been shown to provide highly accurate water vapor profiles from the midtroposphere to the surface [*Kursinski and Gebhardt*, 2014], with subkilometer vertical resolution [*Kursinski et al.*, 2000]. These profiles have been used to probe the internal humidity structure of tropical cyclones [*Vergados et al.*, 2013], improve understanding of infrared retrievals under cloudy conditions [*Vergados et al.*, 2014], and advance our understanding of how tropical humidity is related to large-scale atmospheric circulation patterns such as the Hadley cell [*Vergados et al.*, 2015]. These circulations can affect the global atmospheric dynamics and thus the global CH_4 distribution. Furthermore, measurements of intense precipitation and other hydrometeors are expected from polarimetric GNSS-RO observations, a concept to be tested from a spaceborne experiment [*Cardellach et al.*, 2014b]. This would represent an additional piece of the hydrological cycle being measured by GNSS-based techniques.

Targeting the annual maximum inundation extent as well as the accumulated duration of flooding for each geographical location are of key importance to improve our understanding of the role of wetlands in the global carbon and energy cycle. With a daily coverage or better, a GNSS-based observation system would have the capacity to provide such critical input, even with a spatial resolution coarser than today's L band SAR systems, the complementarity in the system of systems is evident. Moreover, the global coverage of the GNSS-R would not only allow daily mapping of all the world's wetlands but also provide critical information about boreal freeze/thaw processes and the effects of climate change in subarctic permafrost regions, information which currently is either scarce or lacking.

7.3. Wetland Monitoring and Societal Benefits

Beyond the fundamental science research, wetland information that GNSS-R can contribute to direct societal benefit applications and policy implementation in an array of ecosystem functions where wetlands must be preserved or restored [*Loyola Marymount University*, 2015]. For example, a significant application would be to monitor swamp forests since the plant canopy limits the value of optical and higher frequency (X and C bands) SAR sensors. With a better capability for forest penetration, past and current L band systems such as JERS-1, ALOS, and ALOS-2 have been used to map seasonal inundation dynamics in major tropical and boreal river basins; however, the 6 week temporal resolution has proven insufficient to accurately characterize the complex and highly dynamic flooding patterns across river basins. GNSS-R would support the mapping of inundation patterns in much higher temporal detail, at both pan-basin and subbasin scales and allow detection of key events such as maximum inundation stages (which vary in timing and location across the basins) and irregular episodic flooding due to rain. Monitoring seasonally inundated savannas and papyrus swamps in the Amazon delta and the vast and often inaccessible subarctic wetland and permafrost areas that are particularly susceptible to climate change, are additional examples of important applications. There is also evident potential for much enhanced logistics information for waterway transportation by the ability to see through canopy-hidden floodplains and wetlands and determine if they are flooded or not.

The United Nations Sustainable Development Goals, adopted in 2015, identify 17 goals and a variety of related targets. Target 6.6 is "By 2020, protect and restore water-related ecosystems, including mountains, forests, wetlands, rivers, aquifers, and lakes," and the key indicator identified for monitoring progress toward that goal is "Percentage of change in water-related ecosystems extent over time" [*Inter-Agency and Expert Group on Sustainable Development Goal Indicators*, 2016]. Wetland extent has also been identified by Ramsar as a key variable to monitor [*Ramsar CoP 12*, 2015], and yet the needed observations are not globally or regularly available. Although GNSS-R has a subkilometer resolution (e.g., 0.5–1.0 km for most incidence angles up to 70° with a receiver at an altitude of 500 km like that of CYGNSS), it would still fill a critical information gap and even more so if the resolution could be improved by a synergistic approach. Thus, future wetland observation systems should exploit the synergy by combining GNSS-R data having a high temporal resolution to capture the dynamics with other sensors having a high spatial resolution to account for local wetland features. Note that the median size of all 2200 or so Ramsar sites is about 5400 ha (the average size of about 96,000 ha is skewed by some very large sites). The shape of a site is also important, for roughly

square or circular sites a 0.5 km boundary delimitation uncertainty results in an error in areal extent of about 15–20%.

Finally, the Global Wetland Observing System (GWOS) has been identified by the Ramsar Secretariat as a priority [*Ramsar STRP 19*, 2015] as it would provide regular critical inputs to the State of the World's Wetlands report. However, current observation systems cannot yet provide all the needed inputs for these reports and GWOS remains largely in the concept phase. In view of GWOS, GNSS-R data would provide valuable inputs on a regular and global basis and be a main contributor to the Convention, which is global.

7.4. Urgency in Advancing Wetland Monitoring Capability

There is an urgent demand for a significant advance in wetland monitoring capability, as CH_4 emission has increased again since 2007 after a decade of methane stability (section 1). Closely observing the renewed increase in a timely manner, as CH_4 emission changes along a new phase whose exact cause is yet to be found, is necessary to establish whether it is a part of an ongoing decadal cycle or a shift into a new regime of CH_4 emission.

The urgency of developing a synergistic method to monitor wetlands is emphasized by the rapid rate of wetland loss—roughly 64% of the world's wetlands have disappeared since 1900 [*Ramsar Fact Sheet 3*, 2015]. Tracking the rate of wetland loss and assessing the efficacy of wetland restoration and conservation measures are important beyond their reporting value—these wetlands provide crucial ecosystem services upon which much of humanity depends. It is only with a good understanding of how wetlands are changing that appropriate responses can be implemented. These responses require sound hydrological data and science to address water level control, flood storage, and sustainability of water supply under a changing climate [*Acreman et al.*, 2007].

8. Summary

Monitoring wetland dynamics with a high temporal resolution and a global coverage is critical to fill an important Earth sciences information gap and thereby advance the capability to address science issues in global cycles of energy (methane as a greenhouse gas) and water (terrestrial water storage affecting sea level rise). Current methods including six different categories of satellite sensors are reviewed. In addition, a recent approach based on microwave scatterometer polarization ratio anomalies is used to observe wetland change in the Mississippi floodplain and a delayed response in river discharge, illustrating the capacity and timescale of the water storage function of wetlands.

A new method using the GNSS-R principle is presented with results from the Catalonia flight campaign and from TDS-1 satellite measurements. These demonstrate the potential capability to delineate and map inundated wetland extent and suggest how to provide further improvements. Then, we examine future GNSS-R satellites such as CYGNSS, 3CAT-2, and GEROS-ISS, the latter two also enabling investigations on polarimetric and altimetric techniques. Together with other constellation configurations, GNSS-R measurements can occur in synergy with other existing satellite sensors to advance wetland monitoring.

Finally, the basic and critical need for better wetland monitoring is detailed, both in terms of advancing the science to address methane emission, water, and energy cycle, and for direct societal benefits. As demonstrated with both aircraft and satellite GNSS-R data, inundated wetland can be detected even under dense and thick vegetation. Results presented in this paper, such as the coherency and reflected power levels of different land surface types, quantification of the difference in the GNSS-R signatures of wet and dry land, pair ratio method to account for antenna gain, optimal averaging time interval, potential resolution and coverage will be useful and applicable to future GNSS-R developments. The capability of a future GNSS-R system to provide a breakthrough in global frequent coverage (daily, weekly, and beyond) with a potentially subkilometer resolution for wetland mapping can enable new and major science and application advances. Further analysis is critical, however, in order to determine the optimum measurement suite and satellite configurations to accomplish these objectives most efficiently.

References

Acreman, M. C., J. Fisher, C. J. Stratford, D. J. Mould, and J. O. Mountford (2007), Hydrological science and wetland restoration: Some case studies from Europe, *Hydrol. Earth Syst. Sci.*, *11*(1), 158–169.

Bennett, J. (2016), Big Lake National Wildlife Refuge, in *Encyclopedia of Arkansas History and Culture*, The Central Arkansas Library System, Manila, Ark. [Available at http://www.encyclopediaofarkansas.net/encyclopedia/entry-detail.aspx?entryID=2418, accessed March 2016.]

Birkett, C. M. (1998), Contribution of the TOPEX NASA radar altimeter to the global monitoring of large rivers and wetlands, *Water Resour. Res.*, *34*, 1223–1239, doi:10.1029/98WR00124.

Brakenridge, G. R., and E. Anderson (2006), MODIS-based flood detection, mapping, and measurement: The potential for operational hydrological applications, in *Transboundary Floods: Reducing the Risks Through Flood Management*, edited by J. Marsalek et al., pp. 1–12, Springer, Houten, Dordrecht, Netherlands.

Brakenridge, G. R., S. V. Nghiem, E. Anderson, and S. Chien (2005), Space-based measurement of river runoff, *Eos Trans. AGU*, *86*(19), 185–188, doi:10.1029/2005EO190001.

Brisco, B., N. Short, J. van der Sanden, R. Landry, and D. Raymond (2009), A semi-automated tool for surface water mapping with RADARSAT-1, *Can. J. Remote Sens.*, *35*(4), 336–344.

Camps, A., et al. (2012), Review of the CALIMAS team contributions to European Space Agency's soil moisture and ocean salinity mission calibration and validation, *Remote Sens.*, *4*(5), 1272–1309, doi:10.3390/rs4051272.

Camps, A., H. Park, M. Pablos, G. Foti, C. P. Gommenginger, P. W. Liu, and J. Judge (2016), Sensitivity of GNSS-R spaceborne observations to soil moisture and vegetation, *IEEE J. Sel. Top. Appl. Earth Obs. Remote Sens.*, *99*, 1–13, doi:10.1109/JSTARS.2016.2588467.

Cardellach, E., F. Fabra, O. Nogués-Correig, S. Oliveras, S. Ribó, and A. Rius (2011), GNSS-R ground-based and airborne campaigns for ocean, land, ice and snow techniques: Application to the GOLD-RTR datasets, *Radio Sci.*, *46*, RS0C04, doi:10.1029/2011RS004683.

Cardellach, E., A. Rius, M. Martin-Neira, F. Fabra, O. Nogues-Correig, S. Ribo, J. Kainulainen, A. Camps, and S. Addio (2014a), Consolidating the precision of interferometric GNSS-R ocean altimetry using airborne experimental data, *IEEE Trans. Geosci. Remote Sens.*, *52*(8), 4992–5004, doi:10.1109/TGRS.2013.2286257.

Cardellach, E., et al. (2014b), Sensitivity of PAZ LEO polarimetric GNSS radio-occultation experiment to precipitation events, *IEEE Trans. Geosci. Remote Sens.*, *53*(1), 190–206, doi:10.1109/TGRS.2014.2320309.

Carreño-Luengo, H., A. Camps, I. Perez-Ramos, G. Forte, R. Onrubia, and R. Diez (2013), [3]Cat-2: A P(Y) and C/A GNSS-R experimental nano-satellite mission, in *IEEE International Geoscience and Remote Sensing Symposium, Melbourbe, VIC*, pp. 843–846, IEEE, Melbourne, Australia, doi:10.1109/IGARSS.2013.6721290.

Chapman, B., K. McDonald, M. Shimada, A. Rosenqvist, R. Schroeder, and L. Hess (2015), Mapping regional inundation with spaceborne L-band SAR, *Remote Sens.*, *7*(5), 5440–5470, doi:10.3390/rs70505440.

Chen, W., K. Chen, C. P. Kuang, D. Z. Zhu, L. L. He, X. D. Mao, H. D. Liang, and H. L. Song (2016), Influence of sea level rise on saline water intrusion in the Yangtze River Estuary, China, *Appl. Ocean Res.*, *54*, 12–25, doi:10.1016/j.apor.2015.11.002.

Chew, C. C., E. E. Small, K. M. Larson, and V. U. Zavorotny (2014), Effects of near-surface soil moisture on GPS SNR data: Development of a retrieval algorithm for soil moisture, *IEEE Trans. Geosci. Remote Sens.*, *52*(1), 537–543.

Chew, C. C., E. E. Small, K. M. Larson, and V. U. Zavorotny (2015a), Vegetation sensing using GPS-Interferometric Reflectometry: Theoretical effects of canopy parameters on signal-to-noise ratio data, *IEEE Trans. Geosci. Remote Sens.*, *53*(5), 2755–2764.

Chew, C. C., E. E. Small, and K. M. Larson (2015b), An algorithm for soil moisture estimation using GPS-interferometric reflectometry for bare and vegetated soil, *GPS Solutions*, doi:10.1007/s10291-015-0462-4.

Chew, C. C., R. Shah, C. Zuffada, G. Hajj, D. Masters, and A. J. Mannucci (2016), Demonstrating soil moisture remote sensing with observations from the UK TechDemoSat-1 satellite mission, *Geophys. Res. Lett.*, *43*, 3317–3324, doi:10.1002/2016GL068189.

Clarizia, M. P., C. Ruf, P. Cipollini, and C. Zuffada (2016), First spaceborne observation of sea surface height using GPS-Reflectometry, *Geophys. Res. Lett.*, *43*, 767–774, doi:10.1002/2015GL066624.

Costa, M. P. F., and K. H. Telmer (2006), Utilizing SAR imagery and aquatic vegetation to to map fresh and brakish lakes in the Brazilian Pantanal wetland, *Remote Sens. Environ.*, *105*, 204–213.

Cyclone Global Navigation Satellite System (2015), Cyclone Global Navigation Satellite System (CYGNSS). [Available at http://clasp-research.engin.umich.edu/missions/cygnss/, accessed Sept. 2015.]

De Roo, R. D., and F. T. Ulaby (1994), Bistatic specular scattering from rough dielectric surfaces, *IEEE Trans. Antennas Propag.*, *42*(2), 220–231.

Durack, P. J., S. E. Wijffels, and R. J. Matear (2012), Ocean salinities reveal strong global water cycle intensification during 1950 to 2000, *Science*, *336*(6080), 455–458, doi:10.1126/science.1212222.

Egido, A., S. Paloscia, E. Motte, L. Guerriero, N. Pierdicca, M. Caparrini, E. Santi, G. Fontanelli, and N. Floury (2014), Airborne GNSS-R polarimetric measurements for soil moisture and above-ground biomass estimation, *IEEE J. Sel. Top. Appl. Earth Obs. Remote Sens.*, *7*(5), 1522–1532, doi:10.1109/JSTARS.2014.2322854.

Fabra, F., E. Cardellach, A. Rius, S. Ribo, S. Oliveras, O. Nogues-Correig, M. B. Rivas, M. Semmling, and S. D'Addio (2011), Phase altimetry with dual polarization GNSS-R over sea ice, *IEEE Trans. Geosci. Remote Sens.*, *50*(6), 2112–2121, doi:10.1109/TGRS.2011.2172797.

Ferrazzoli, P., L. Guerriero, N. Pierdicca, and R. Rahmoune (2011), Forest biomass monitoring with GNSS-R: Theoretical simulations, *Adv. Space Res.*, *47*(10), 1823–1832, doi:10.1016/j.asr.2010.04.025.

Foti, G., C. Gommenginger, P. Jales, M. Unwin, A. Shaw, C. Robertson, and J. Rosello (2015), Spaceborne GNSS reflectometry for ocean winds: First results from the UK TechDemoSat-1 mission, *Geophys. Res. Lett.*, *42*, 5435–5441, doi:10.1002/2015GL064204.

Fuks, I. M., and A. G. Voronovich (2000), Wave diffraction by rough interfaces in an arbitrary plane-layered medium, *Waves Random Media*, *10*, 37–41.

Fish and Wildlife Service (FWS) (2016a), Big Lake National Wildlife Refuge, U. S. Fish and Wildl. Serv. [Available at http://www.fws.gov/biglake/, accessed March 2016.]

Fish and Wildlife Service (FWS) (2016b), National wetlands inventory, U. S. Fish & Wildl. Serv. [Available at http://www.fws.gov/wetlands/data/mapper.HTML, accessed Jan. 2016.]

Garrison, J. L., and S. J. Katzberg (2000), The application of reflected GPS signals to ocean remote sensing, *Remote Sens. Environ.*, *73*(2), 175–187.

Garrison, J. L., A. Komjathy, V. U. Zavorotny, and S. J. Katzberg (2002), Wind speed measurement using forward scattered GPS signals, *IEEE Trans. Geosci. Remote Sens.*, *40*(1), 50–65, doi:10.1109/36.981349.

Gornitz, V., C. Rosenzweig, and D. Hillel (1997), Effects of anthropogenic intervention in the land hydrologic cycle on global sea level rise, *Global Planet. Change*, *14*(3–4), 147–161, doi:10.1016/S0921-8181(96)00008-2.

Hajj, G. A., and C. Zuffada (2003), Theoretical description of a bistatic system for ocean altimetry using the GPS signal, *Radio Sci.*, *38*(5), 1089, doi:10.1029/2002RS002787.

Hall, C., and R. Cordey (1988), Multistatic scatterometry, in *Proceedings of the IEEE International Geoscience Remote Sensing Symposium, 13–16 Sep.*, pp. 561–562, Edinburgh.

Hallikainen, M. T., F. T. Ulaby, M. C. Dobson, M. A. El-Rayes, and L.-K. Wu (1985), Microwave dielectric behavior of wet soil-part 1: Empirical models and experimental observations, *IEEE Trans. Geosci. Remote Sens.*, *GE-23*(1), 25–34.

Henderson, F., and A. Lewis (2008), Radar detection of wetland ecosystems: A review, *Int. J. Remote Sens.*, *29*(20), 5809–5835.

Hestir, E. L., V. E. Brando, M. Bresciani, C. Giardino, E. Matta, P. Villa, and A. G. Dekker (2015), Measuring freshwater aquatic ecosystems: The need for a hyperspectral global mapping satellite mission, *Remote Sens. Environ.*, *167*, 181–195, doi:10.1016/j.rse.2015.05.023.

Hoekman, D. (2007), Satellite radar observation of tropical peat swamp forest as a tool for hydrological modelling and environmental protection, *J. Aquat. Conserv. Mar. Freshwater Ecosyst.*, *17*(3), 265–275.

Inter-Agency and Expert Group on Sustainable Development Goal Indicators (2016), Report of the Inter-Agency and Expert Group on Sustainable Development Goal Indicators (Annex III), UN Econ. and Social Counc., Stat. Comm., 47th Session, 8–11 March. [Available at http://unstats.un.org/unsd/statcom/47th-session/documents/2016-2-SDGs-Rev1-E.pdf, accessed June 2016].

Institut Cartogràfic i Geològic de Catalunya (2015), VISSIR v3.26. [Available at http://www.icc.cat/vissir3/, accessed Aug. 2015.]

Intergovernmental Panel on Climate Change (IPCC) (2013), *Climate Change 2013: The Physical Science Basis, Contribution of Working Group I to the Fifth Assessment Report of the Intergovernmental Panel on Climate Change*, edited by T. F. Stocker et al., 1535 pp., Cambridge Univ. Press, Cambridge, U. K.

International Geosphere-Biosphere Programme-Global Analysis, Interpretation and Modelling (IGBP-GAIM) (1996), *Global Wetland Distribution and Functional Characterization: Trace Gases and the Hydrological Cycle, IGBP-GAIM Rep. 2*, 40 pp., edited by D. Sahagian and J. Melack, Santa Barbara, Calif.

Japan Aerospace Exploration Agency Earth Observing Research Center (2016), The ALOS Kyoto & Carbon Initiative. [Available at http://www.eorc.jaxa.jp/ALOS/en/kyoto/kyoto_index.htm, accessed June 2016.]

Kaatze, U. (1989), Complex permittivity of water as a function of frequency and temperature, *J. Chem. Eng. Data*, *34*(4), 371–374.

Katzberg, S. J., O. Torres, M. S. Grant, and D. Masters (2006), Utilizing calibrated GPS reflected signals to estimate soil reflectivity and dielectric constant: Results from SMEX02, *Remote Sens. Environ.*, *100*(1), 17–28, doi:10.1016/j.rse.2005.09.015.

Kumar, V., M. Kumari, and S. K. Saha (2016), Discrimination of basmati and non-basmati rice types using polarimetric target decomposition of temporal SAR data, *Curr. Sci.*, *110*(11), 2166–2169, doi:10.18520/cs/v110/i11/2166-2169.

Kursinski, E. R., and T. Gebhardt (2014), A method to deconvolve errors in GPS RO-derived water vapor histograms, *J. Atmos. Oceanic Technol.*, *31*(12), 2606–2628.

Kursinski, E. R., G. A. Hajj, S. S. Leroy, and B. Herman (2000), The GPS radio occultation technique, *Terr. Atmos. Oceanic Sci.*, *11*(1), 53–114.

Le Toan, T., F. Ribbes, N. Floury, L. Wang, J. A. Kong, T. Kurosu, and M. Fujita (1997), Rice crop mapping and monitoring using ERS-1 data based on experiment and modeling results, *IEEE Trans. Geosci. Remote Sens.*, *35*(1), 41–56.

Loyola Marymount University (2015), The Ballona Wetlands: Nature's water treatment system, Loyola Marymount Univ., Cent. for Urban Resilience. [Available at http://cures.lmu.edu/blog/the-ballona-wetlands-natures-water-treatment-system/, accessed Oct. 2015.]

Lowe, S. T., C. Zuffada, Y. Chao, P. Kroger, L. E. Young, and J. L. LaBrecque (2002), 5-cm-precision aircraft ocean altimetry using GPS reflections, *Geophys. Res. Lett.*, *29*(10), 1375, doi:10.1029/2002GL014759.

Mañosa, S., R. Mateo, and R. Guitart (2001), A review of the effects of agricultural and industrial contamination on the Ebro delta biota and wildlife, *Environ. Monit. Assess.*, *71*(2), 187–205, doi:10.1023/A:1017545932219.

Martín-Neira, M. (1993), A passive reflectometry and interferometry system (PARIS): Application to ocean altimetry, *ESA J.*, *17*, 331–355.

Matthews, E., and I. Fung (1987), Methane emission from natural wetlands: Global distribution, area, and environmental characteristics of sources, *Global Biogeochem. Cycles*, *1*, 61–86, doi:10.1029/GB001i001p00061.

Melack, J. (2004), Remote sensing of tropical wetlands, in *Manual of Remote Sensing, Remote Sensing for Natural Resources Management and Environmental Monitoring*, vol. 4, edited by S. Ustin, pp. 319–343, Wiley, New York.

Mermoz, S., M. Réjou-Méchain, L. Villard, T. Le Toan, V. Rossi, and S. Gourlet-Fleury (2015), Decrease of L-band SAR backscatter with biomass of dense forests, *Remote Sens. Environ.*, *159*, 307–317, doi:10.1016/j.rse.2014.12.019.

Measurement of Earth Reflected Radio-navigation Signals by Satellite (2015), Measurement of Earth Reflected Radio-navigation Signals by Satellite. [Available at http://www.merrbys.org/, accessed Mar. 2015.]

Miguez-Macho, G., and Y. Fan (2012), The role of groundwater in the Amazon water cycle: 1. Influence on seasonal streamflow, flooding and wetlands, *J. Geophys. Res.*, *117*, D15113, doi:10.1029/2012JD017539.

Moré, G., P. Serra, and X. Pons (2011), Multitemporal flooding dynamics of rice fields by means of discriminant analysis of radiometrically corrected remote sensing imagery, *Int. J. Remote Sens.*, *32*(7), 1983–2011, doi:10.1080/01431161003645816.

Moser, L., A. Schmitt, A. Wendleder, and A. Roth (2016), Monitoring of the Lac Bam wetland extent using dual-polarized X-Band SAR data, *Remote Sens.*, *8*(4), Article 302, doi:10.3390/rs8040302.

Nelson, S. O. (1991), Dielectric properties of agricultural products-measurements and applications, *IEEE Trans. Instrum. Meas.*, *41*(1), 385–387.

Neumann, B., A. T. Vafeidis, J. Zimmermann, and R. J. Nicholls (2015), Future coastal population growth and exposure to sea-level rise and coastal flooding—A global assessment, *PLoS One*, *10*(3), e0118571, doi:10.1371/journal.pone.0118571.

Nghiem, S. V. (2001), Advanced scatterometry for geophysical remote sensing, Tech. Rep., 39 pp., Jet Prop. Lab., Calif. Inst. of Technol., Pasadena.

Nguyen, D. B., K. Clauss, S. M. Cao, V. Naeimi, C. Kuenzer, and W. Wagner (2015), Mapping rice seasonality in the Mekong Delta with multi-year Envisat ASAR WSM data, *Remote Sens.*, *7*(12), 15,868–15,893, doi:10.3390/rs71215808.

Nguyen, L. D., T. Le Toan, A. Apan, A. Bouvet, F. Young, and L. V. Trung (2009), Effects of changing rice cultural practices on C-band synthetic aperture radar backscatter using Envisat advanced synthetic aperture radar data in the Mekong River Delta, *J. Appl. Remote Sens.*, *3*, 033563, doi:10.1117/1.3271046.

Papa, F., C. Prigent, F. Aires, C. Jimenez, W. B. Rossow, and E. Matthews (2010), Interannual variability of surface water extent at the global scale, 1993–2004, *J. Geophys. Res.*, *115*, D12111, doi:10.1029/2009JD012674.

Pierdicca, N., L. Guerriero, M. Brogioni, and A. Egido (2012), On the coherent and non coherent components of bare and vegetated terrain bistatic scattering: Modelling the GNSS-R signal over land, in *Proceedings of the IEEE International Geoscience and Remote Sensing Symposium, 22–27 July*, pp. 3407–3410, IEEE, Munich, Germany.

Ramsar Convention (2015), The Ramsar convention on wetlands. [Available at http://www.ramsar.org/, accessed Feb. 2015.]

Ramsar CoP 12 (2015), Resolution XII.5 (Annex 3), Punta del Este, Uruguay, 1–9 June. [Available at http://www.ramsar.org/sites/default/files/documents/library/cop12_res05_new_strp_e_0.pdf, accessed June 2016.]

Ramsar Fact Sheet 3 (2015), Wetlands: A global disappearing act, Ramsar Convention on Wetlands. [Available at http://www.ramsar.org/sites-countries/ramsar-fact-sheets, accessed Feb. 2015.]

Ramsar STRP 19 (2015), Convention on Wetlands (Ramsar, Iran, 1971) 19th Meeting of the Scientific and Technical Review Panel (STRP), Gland, Switzerland, 2–6 Nov. [Available at http://www.ramsar.org/sites/default/files/documents/library/211202_strp19_report.pdf, accessed June 2016.]

Rebelo, L. M. (2015), Eco-hydrological characterization of inland wetlands in Africa using L-Band SAR, *IEEE J. Sel. Top. Appl. Earth Obs. Remote Sens.*, *3*(4), 554–559, doi:10.1109/JSTARS.2010.2070060.

Ribó, S., J. C. Arco Fernandez, S. Oliveras, E. Cardellach, A. Rius, and C. Buck (2014), Experimental results of an X-band PARIS receiver using digital satellite TV opportunity signals scattered on the sea surface, *IEEE Trans. Geosci. Remote Sens.*, *52*(9), 5704–5711, doi:10.1109/TGRS.2013.2292007.

Rius, A., E. Cardellach, and M. Martín-Neira (2010), Altimetric analysis of the sea-surface GPS-reflected signals, *IEEE Trans. Geosci. Remote Sens.*, *48*(4–2), 2119–2127.

Rodriguez-Alvarez, N., X. Bosch-Lluis, A. Camps, M. Vall-Ilossera, E. Valencia, J. F. Marchan-Hernandez, and I. Ramos-Perez (2009), Soil moisture retrieval using GNSS-R techniques: Experimental results over a bare soil field, *IEEE Trans. Geosci. Remote Sens.*, *47*(11), 3616–3624, doi:10.1109/TGRS.2009.2030672.

Rokni, K., A. Ahmad, A. Selamat, and S. Hazini (2014), Water feature extraction and change detection using Multitemporal Landsat Imagery, *Remote Sens.*, *6*(5), 4173–4189, doi:10.3390/rs6054173.

Romanov, A. N., and I. V. Khvostov (2015), Microwave remote monitoring of Altai catastrophic flood dynamics using SMOS Data, *IEEE Geosci. Remote Sens. Lett.*, *12*(10), 2036–2040, doi:10.1109/LGRS.2015.2444592.

Rosenqvist, A., B. Forsberg, T. Pimentel, Y. Rauste, and J. Richey (2002), The use of spaceborne radar data to model inundation patterns and trace gas emissions in the Central Amazon floodplain, *Int. J. Remote Sens.*, *23*(7), 1303–1328.

Rosenqvist, A., M. Finlayson, J. Lowry, and D. Taylor (2007), The potential of long wavelength satellite borne radar to support implementation of the Ramsar Wetlands Convention, *J. Aquat. Conserv. Mar. Freshwater Ecosyst.*, *17*(3), 229–244.

Ruf, C., et al. (2016a), New ocean winds satellite mission to probe hurricanes and tropical convection, *Bull. Am. Meteorol. Soc.*, *97*(3), 385–395, doi:10.1175/BAMS-D-14-00218.1.

Ruf, C., et al. (2016b), *CYGNSS Handbook*, 154 pp., Mich. Publ., Ann Arbor.

Sahagian, D. (2000), Global physical effects of anthropogenic hydrological alterations: Sea level and water redistribution, *Global Planet. Change*, *25*(1–2), 39–48, doi:10.1016/S0921-8181(00)00020-5.

Santoro, M., U. Wegmuller, C. Lamarche, S. Bontemps, P. Defourny, and O. Arino (2015), Strengths and weaknesses of multi-year Envisat ASAR backscatter measurements to map permanent open water bodies at global scale, *Remote Sens. Environ.*, *171*, 185–201, doi:10.1016/j.rse.2015.10.031.

Shah, R., J. L. Garrison, and M. S. Grant (2012), Demonstration of bistatic radar for ocean remote sensing using communication satellite signals, *IEEE Geosci. Remote Sens. Lett.*, *9*(4), 619–623, doi:10.1109/LGRS.2011.2177061.

Silva, T., M. Costa, and J. Melack (2010), Spatio-temporal variability of macrophyte cover and productivity in the eastern Amazon floodplain: A remote sensing approach, *Remote Sens. Environ.*, *114*(9), 1998–2010.

Slater, J. A., G. Garvey, C. Johnston, J. Haase, B. Heady, G. Kroenung, and J. Little (2006), The SRTM data "finishing" process and products, *Photogramm. Eng. Remote Sens.*, *72*(3), 237–247.

Small, E. E., K. M. Larson, C. C. Chew, J. Dong, and T. E. Ochsner (2016), Validation of GPS-IR soil moisture retrievals: Comparison of different algorithms to remove vegetation effects, *IEEE J. Sel. Top. Appl. Earth Obs. Remote Sens.*, *99*, 1–12, doi:10.1109/JSTARS.2015.2504527.

Shuttle Radar Topography Mission (2014), Shuttle Radar Topography Mission, the mission to map the world. [Available at http://www2.jpl.nasa.gov/srtm/, accessed Aug. 2015.]

Surrey (2015), ESA TDS-1 GNSS-R exploitation study, Doc. No. SS E P -#0248344, 20 pp., Surrey Satell. Technol. Ltd., revision release 4 Mar. 2015.

Syed, T. H., J. S. Famiglietti, D. P. Chambers, J. K. Willis, and K. Hilburn (2010), Satellite-based global-ocean mass balance estimates of inter-annual variability and emerging trends in continental freshwater discharge, *Proc. Natl. Acad. Sci. U. S. A.*, *107*(42), 17,916–17,921, doi:10.1073/pnas.1003292107.

Toyra, J., A. Pietroniro, L. W. Martz, and T. D. Prowse (2002), A multi-sensor approach to wetland flood monitoring, *Hydrol. Processes*, *16*(8), 1569–1581, doi:10.1002/hyp.1021.

Ulaby, F. T., and M. A. El-Rayes (1987), Microwave dielectric spectrum of vegetation—part II: Dual-dispersion model, *IEEE Trans. Geosci. Remote Sens.*, *GE-25*(5), 550–557.

USGS (2016), EDNA derived watersheds for major named rivers. U. S. Geol. Surv. [Available at http://edna.usgs.gov/watersheds/html_index.htm, accessed March 2016.]

Vergados, P., A. J. Mannucci, and H. Su (2013), A validation study for GPS radio occultation data with moist thermodynamic structure of tropical cyclones, *J. Geophys. Res. Atmos.*, *118*, 9401–9413, doi:10.1002/jgrd50698.

Vergados, P., A. J. Mannucci, and C. O. Ao (2014), Assessing the performance of GPS radio occultation measurements in retrieving tropo-spheric humidity in cloudiness: A comparison study with radiosondes, ERA-Interim, and AIRS data sets, *J. Geophys. Res. Atmos.*, *119*, 7718–7731, doi:10.1002/2013JD021398.

Vergados, P., A. J. Mannucci, C. O. Ao, J. H. Jiang, and H. Su (2015), On the comparisons of tropical relative humidity in the lower and middle troposphere among COSMIC radio occultations and MERRA and ECMWF data sets, *Atmos. Meas. Tech.*, *8*(4), 1789–1797, doi:10.5194/amt-8-1789-2015.

VTV1 (2012), Strange lake, N. Q. Phong, Production Dir., Discovering Vietnam, Ep. 98. [Available at https://www.youtube.com/watch?v=rd0bXfgZaGQ, accessed Jan. 2015.]

Watts, J. D., J. S. Kimball, L. A. Jones, R. Schroeder, and K. C. McDonald (2012), Satellite Microwave remote sensing of contrasting surface water inundation changes within the Arctic-Boreal Region, *Remote Sens. Environ.*, *127*, 223–236, doi:10.1016/j.rse.2012.09.003.

Weatherall, P., M. Marks, K. M. Jakobsson, T. Schmitt, S. Tani, J. E. Arndt, M. Rovere, D. Chayes, V. Ferrini, and R. Wigley (2015), A new digital bathymetric model of the world's oceans, *Earth Space Sci.*, *2*(8), 331–345, doi:10.1002/2015EA000107.

Whitaker, S. (1986), Flow in porous media I: A theoretical derivation of Darcy's law, *Transp. Porous Media*, *1*(1), 3–25, doi:10.1007/BF01036523.

Whitcomb, J., M. Moghaddam, K. McDonald, and J. Kellndorfer (2007), Wetlands map of Alaska using L-Band radar satellite imagery, in *Proceedings of the IEEE International Geoscience and Remote Sensing Symposium (IGARSS), July 23–28, 2007*, pp. 2487–2490, Barcelona, Spain.

Wickert, J., et al. (2016), Innovative sea surface monitoring with GNSS-REflectometry aboard ISS: Overview and recent results from GEROS-ISS, in *Proceedings of the 2016 IEEE International Geoscience and Remote Sensing Symposium (IGARSS)*, pp. 5611–5612, Beijing, China, doi:10.1109/IGARSS.2016.7730465.

Zavorotny, V. U., and A. G. Voronovich (2000), Scattering of GPS signals from the ocean with wind remote sensing application, *IEEE Trans. Geosci. Remote Sens.*, *38*(2), 951–964, doi:10.1109/36.841977.